From the holdings of the Department of Special Collections , Princeton University Library, Princeton, NJ

These documents are either in the public domain, or can only be used for educational and research purposes (Fair use) as per U.S. Copyright law (text below). By accessing this file, all users agree that their use falls in the public domain or within fair use as defined by the copyrightlaw. We do not charge any permission or usage fees for the publication of images of material inour collections, including those provided by Princeton University Library, via our website, catalog, or directly from staff.For more information regarding copyright, credit, and citation please review the information onthe Copyright, Credit and Citation Guidelines page of our website.
https://library.princeton.edu/special-collections/policies/copyright-credit-and-citation-guidelines. If you have any questions, including how to order higher-quality images from the collection, contact Special Collections Public Services via our Ask Us! Form. https://library.princeton.edu/special-collections/ask-us

---

Master's Theses, 2022-2026 Chemical and Biological Engineering

2025

Reactor modeling for thin film diamond growth

Paragian, Kristin

Princeton, NJ : Princeton University

---

http://arks.princeton.edu/ark:/88435/dsp015m60qw34p

U.S. Copyright law: The copyright law of the United States (Title 17, §108, United States Code) governs the making of photocopies or other reproductions of copyrighted material. Under certain conditions specified in the law, libraries and archives are authorized to furnish a photocopy or other reproduction. One of these specified conditions is that the photocopy or reproduction is not to be used for any purpose other than private study, scholarship, or research. If a user makes a request for, or later uses, a photocopy or reproduction for purposes in excess of fair use that user may be liable for copyright infringement. This institution reserves the right to refuse to accept a copying order if, in its judgment, fulfillment of the order would involve a violation of copyright law. https://www.copyright.gov/title17/title17.pdf

REACTOR MODELING FOR THIN FILM DIAMOND GROWTH

Kristin Paragian

A MASTER'S THESIS

PRESENTED TO THE FACULTY

OF PRINCETON UNIVERSITY

IN CANDIDACY FOR THE DEGREE

OF MASTER OF SCIENCE IN ENGINEERING

RECOMMENDED FOR ACCEPTANCE BY

THE DEPARTMENT OF

CHEMICAL AND BIOLOGICAL ENGINEERING

Adviser: David B. Graves

May 2025

© Copyright by Kristin Paragian, 2025. All rights reserved.

Abstract

Diamond has impressive physical properties, including the highest thermal conductivity of any material, chemical inertness, hardness, and refractive index, among others. Diamond films can be deposited today with these desirable properties but only over relatively small areas (~ 5 cm^2). Applications in microelectronics require uniform deposition over 300 mm diameter silicon wafers. One possibility to scale diamond growth reactors to higher areas is to exploit parallel plate electrode, capacitively coupled shower head flow plasma reactors. This work explores this concept with a two-dimensional cylindrical model of a parallel plate chemical vapor deposition (CVD) reactor of diamond film growth. The model couples species transport, fluid dynamics, heat transfer, and chemistry for CH_4/H_2 gases. The assumed radial profile of power deposition into the plasma is predicted to be the most important factor governing the radial growth rate uniformity. Another central component of the analysis is a comparison between model-predicted equilibrium and equilibrium mole fractions of key species. The results show that CH_3 and CH_4 remain in local chemical equilibrium throughout the reactor except very near the substrate surface. H and H_2 deviate significantly from local chemical equilibrium due to relatively fast diffusion and slow reaction kinetics. This nonequilibrium in H affects the formation of CH_3 and ultimately impacts the predicted growth rate and defect radial distributions across the wafer diameter. Parametric studies assess the influence of power, pressure, gap size, flow rate, and CH_4 inlet profile. Current generation microwave plasma CVD (MPCVD) reactors demonstrate higher growth rates of diamond film per unit power delivered than the modeled parallel plate reactor design. By contrast, the parallel plate configuration explored here is predicted to deliver higher film growth rates per unit of CH_4 utilized. A combined optimized case, featuring radially uniform power deposition, high gas flow, and increased power, yielded the most radially uniform and highest magnitude growth rate. These results provide design insights for scalable and efficient diamond CVD reactors.

Contents

Abstract **3**

1 Introduction **5**

2 Description of the model **7**

3 Results and discussion **12**
3.1 Base simulation 12
3.2 Effects of altering pressure, power magnitude, and gap size 24
3.3 Effect of improving power uniformity 26
3.4 Effect of increasing inlet flow rate 28
3.5 Effect of altering CH_4 concentration profile at the inlet 31
3.6 Effect of decreasing the maximum temperature 34
3.7 Processing efficiency compared to MPCVD reactor 36
3.8 Comparison of chemical species results and growth rates to MPCVD reactor 37
3.9 Heat flow to the substrate 39
3.10 Combined effects for optimized growth 40

4 Conclusion **43**

Appendices **48**

A Additional equation information **48**

B Comparison of model species densities to the literature **48**

C 2D mole fractions profiles of CH_2, CH, C, C_2H, C_2H_4, C_2H_5, and C_2H_6 **50**

1 Introduction

Diamond has become an attractive material for applications such as electronics, quantum computers, and optics due to its impressive physical properties [1, 2]. Diamond is the most thermally conductive material, with a thermal conductivity of up to 2000 $\frac{\mathrm{W}}{\mathrm{m \cdot K}}$. This is an especially useful property in high-power electronics, such as high-frequency transistors, to efficiently dissipate heat [1]. Common materials used in electronics include copper and silicon carbide, which have thermal conductivities of 398 $\frac{\mathrm{W}}{\mathrm{m \cdot K}}$ and 270 $\frac{\mathrm{W}}{\mathrm{m \cdot K}}$, respectively [3]. Diamond is also highly chemically inert, making it ideal for applications that require stability and commonly cause corrosion in materials, such as quantum computers. Other common materials for these applications are copper, which is susceptible to corrosion in harsh environments and silicon, which readily oxidizes [4, 5]. Diamond's high durability, which is due to its high hardness of 80-100 GPa, is ideal for cutting tools, quantum sensors, and coatings for optics [1]. Common materials for these applications are cubic boron nitride and titanium diboride, with hardnesses of 70 GPa and 25 GPa, respectively [6, 7]. Lastly, diamond's refractive index of 2.41 further supports its use in optics [1]. Glass is a common material used in optics, but only has a refractive index of approximately 1.5 [8].

As electronics and quantum devices become more powerful, it is necessary to use materials that offer exceptional physical qualities. A limiting factor to advancing electronics is heat dissipation. Computer chips, for example, which are commonly made from silicon, must be able to dissipate heat to ensure the device does not break down. Newer electronics, however, are requiring more heat dissipation than silicon can effectively transfer [9]. Diamond, the most thermally conductive material in the world, is capable of handling and dissipating high levels of heat due to its thermal conductivity and hardness. Silicon-based semiconductors are also reaching their physical limits, but boron or phosphorus doped diamond can induce semiconducting qualities, further supporting the incorporation of diamond into electronics [10, 11].

Synthesis of diamond began in the mid 1950s with high pressure, high temperature (HPHT) techniques, wherein the extreme conditions cause the carbon source to dissolve in a metal catalyst, commonly referred to as a solvent-catalyst, where the diamond growth takes place [12, 13]. There

are disadvantages to using HPHT for diamond growth, such as difficulties in growing high purity diamond, which is essential for electronic and optical applications [14]. Additionally, the growth rate of diamond by HPHT has been found to decrease as the diamond gets larger, leading to increased time and cost associated with production and limitations on the size of diamond produced [13]. Chemical vapor deposition (CVD), on the other hand, is a scalable process that produces high quality diamond under less extreme conditions, which is essential for quantum and microelectronic device applications of diamond [12].

CVD of diamond begins with gaseous reactants, typically hydrogen with a small amount of methane (usually less than 5%) [15, 16]. In standard CVD, these reactants are thermally activated to dissociate them into reactive atoms/molecules, such as methyl radicals and hydrogen atoms, which are the dominant species that contribute to diamond growth. Hydrogen atoms terminate the diamond lattice to prevent the diamond from converting to graphite or other carbon structures. Gaseous hydrogen atoms abstract the surface hydrogen atoms to create free radical sites that carbon-containing radicals can adsorb to. The newly adsorbed carbon is fully incorporated into the diamond lattice by further hydrogen abstraction from gaseous hydrogen atoms [16]. It has been well established that plasmas can assist the diamond growth [17–19]. Hot electrons are generated by the plasma, which can transfer energy to heavy species and induce thermal dissociation.

A common reactor to generate diamond is a microwave plasma reactor [15, 16, 20]. Microwave energy, typically at 2.45 GHz, is used to excite the plasma within a resonant cavity. While MPCVD reactors have been well documented for diamond growth, they have only been used to grow diamond up to a few centimeters in diameter [21]. For microelectronics applications, however, diamond must be grown over 300 mm diameter silicon wafers. In this work, we use a parallel plate configuration to grow larger area diamond. The parallel plate configuration consists of a powered upper electrode and a grounded lower electrode. A plasma is formed in between these electrodes, where it thermally activates the gaseous species. In both the MPCVD reactor and the parallel plate configuration, the plasma is located directly above the substrate, and input species are introduced above the plasma region.

For CVD diamond to find use in electronics and quantum devices, the cost of production must be reduced. Costs of CVD diamond production include fixed costs and costs of energy and process gases. Minimizing energy and process gas costs requires maximizing the process efficiency of converting raw feedstock into diamond [22]. Additionally, it is important to understand how reactor conditions affect the quality of diamond grown.

In this work, I develop a detailed understanding of the parallel plate reactor. A base case simulation is used to understand the chemistry of the reactor and how it compares to equilibrium. This simulation also provides a basis for the growth rate and defect ratio. Conditions of the reactor are then changed one by one to explore how growth rate and defects may be improved. Additionally, based on the base case results, the parallel plate reactor is compared with the more traditional MPCVD reactor in terms of processing efficiency and chemical species profiles.

2 Description of the model

The diamond growth reactor is modeled in a 2D cylindrical coordinate system where cylindrical symmetry is assumed, as shown in Figure 1. A powered upper electrode is a distance of 3 cm from a grounded lower electrode. A plasma is formed between these electrodes, where the gas is heated. Due to the strong exponential dependence of the ionization rates and electron density on the reduced electric field E/N, both E/N and the average electron temperature are typically uniformly distributed throughout the plasma region. With this assumption, power absorption and plasma volume can be included as parameters of the model without the need to solve electromagnetic equations [15].

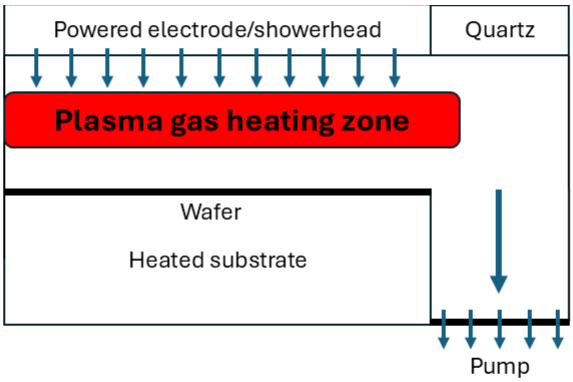

Figure 1: Simulation domain for two-dimensional cylindrical model.

Twelve chemical species are considered: H_2, H, CH_4, CH_3, CH_2, CH, C, C_2H, C_2H_2, C_2H_4, C_2H_5, and C_2H_6. The governing equations consist of a steady state continuity equation for each species, energy balance, and non-isothermal Navier-Stokes:

$$\nabla \cdot (-D_s N \nabla x_s + N \boldsymbol{v} x_s) = S_s \tag{1}$$

$$\nabla \cdot [\sum_s \boldsymbol{\Gamma_s} (C_s T + H_{0,s}) - \lambda \nabla T] = Q \tag{2}$$

$$\rho (\boldsymbol{v} \cdot \nabla) \boldsymbol{v} = \nabla \cdot [-p\boldsymbol{I} + \boldsymbol{K}] \tag{3}$$

$$\nabla \cdot (\rho \boldsymbol{v}) = 0 \tag{4}$$

The subscript s denotes the sth species. D, N, x, $\boldsymbol{v}$, and S are the diffusion coefficient, total particle density, mole fraction, fluid velocity, and source term, respectively. A detailed explanation of how diffusion coefficients are calculated is included in Appendix A.

The total particle density is obtained from the ideal gas law:

$$N = \frac{p}{k_B T} \tag{5}$$

where p, k_B, and T are the gas pressure, Boltzmann constant, and gas temperature, respectively. The terms in parentheses on the left-hand side of Equation 1 denote the total particle flux of species s. $\mathbf{\Gamma}$, C, H_0, λ, and Q are the total particle flux, heat capacity, enthalpy at absolute zero, thermal conductivity, and rate of energy transfer from electrons to heavy species, respectively. ρ, $\boldsymbol{K}$, and $\boldsymbol{F}$ are the gas density, viscous forces, and external forces, respectively.

The viscous forces are calculated according to Equation 6:

$$\boldsymbol{K} = \mu(\nabla \boldsymbol{v} + (\nabla \boldsymbol{v})^T) - \frac{2}{3}\mu(\nabla \cdot \boldsymbol{u})\boldsymbol{I} \tag{6}$$

where μ is the viscosity of H_2.

Heat capacities and thermal conductivities with respect to temperature were obtained from external data [23–25]. It is assumed that the temperature profile does not depend on the carbon chemistry and can be approximated using only hydrogen species. Due to limited data availability and because H_2 is the dominant species in the reactor, the reactor thermal conductivity was assumed to be equal to H_2's thermal conductivity. Data could only be obtained up to 2000 K and was assumed to follow a linear trend beyond that.

The mole fractions of H_2 and CH_4 at the inlet are 0.96 and 0.04, respectively. All other inlet mole fractions are zero. Flux boundary conditions are used for H and CH_3 at the substrate surface. The flux of H into the substrate is computed as

$$\Gamma_{H,\perp} = \frac{1}{4}\gamma_H n_H \bar{v}_H \tag{7}$$

where γ_H, n_H, and $\bar{v}_H$ are the surface reaction probability, number density, and mean molecular speed of H, respectively. The value of γ_H is approximately 0.1 at the substrate temperature on a diamond surface [26].

The flux of CH_3 into the substrate is derived from the growth rate expression proposed by Goodwin in units of $\frac{\mu\text{m}}{\text{hr}}$ [22]:

$$G = 1.8x10^{11} \frac{[CH_3][H]}{5x10^{-9} + [H]} \tag{8}$$

where the concentrations are in units of $\frac{\text{mol}}{\text{cm}^3}$. This growth rate is converted to a CH_3 flux by multiplying it with the diamond density (0.2939 $\frac{\text{mol}}{\text{cm}^3}$), Avogadro's number, and the appropriate scaling factors to obtain flux units of $\frac{1}{\text{m}^2 \cdot \text{s}}$:

$$\Gamma_{CH_3,\perp} = 8.85x10^{30} \frac{[CH_3][H]}{5x10^{-9} + [H]} \tag{9}$$

The diffusive flux of each species is equal to zero at the outlet. All other boundaries use a zero total particle flux boundary condition. The substrate temperature is set to 1200 K, and all exterior walls are set to 600 K, which has been justified previously through experimental measurements [27]. For the Navier-Stokes equation, the inlet velocity and outlet pressure are specified. All other boundaries use a no slip boundary condition.

The reactions and their rate coefficients are listed in Table 1. The preexponential factor, A, has units of $\frac{\text{cm}^3}{\text{mol} \cdot \text{s}}$ or $\frac{\text{cm}^6}{\text{mol}^2 \cdot \text{s}}$ depending on whether it is a two-body or three-body reaction. The rate constants have an Arrhenius form:

$$k = AT^b e^{\frac{-E_A}{RT}} \tag{10}$$

The rate coefficients for reactions 0-3 were taken from Scott et. al. [28]. The forward rate coefficients for reactions 4-18 were taken from Cantera [29]. Reverse rate constants for reactions 4-18 were obtained by fitting equilibrium constants as a function of temperature from Cantera to derive an analytical expression. Reverse rate constants were calculated by dividing the forward rate constant with the temperature-dependent equilibrium constant expression, i.e.:

$$k_{reverse} = \frac{k_{forward}}{K_{eq}} \tag{11}$$

The reduced set of reactions listed in Table 1 was chosen to ensure reasonable agreement with axial

Table 1: Reactions and their corresponding rate coefficients.

No.	Reaction	A ($\frac{cm^3}{mol\ s}$ or $\frac{cm^6}{mol^2 s}$)	b	E_A ($\frac{J}{mol}$)
R0	$2H + H_2 \rightarrow H_2 + H_2$	$1.00x10^{17}$	-0.60	0
R1	$H_2 + H_2 \rightarrow 2H + H_2$	$8.47x10^{17}$	-0.70	$4.367x10^5$
R2	$2H + H \rightarrow H_2 + H$	$3.20x10^{15}$	0	0
R3	$H_2 + H \rightarrow 2H + H$	$2.71x10^{16}$	-0.10	$4.367x10^5$
R4	$CH_4 + H \leftrightarrow CH_3 + H_2$	$6.60x10^8$	1.62	$4.535x10^4$
R5	$CH_3 + H\ (+ H_2) \leftrightarrow CH_4\ (+ H_2)$	$2.62x10^{33}$	-4.76	$1.021x10^4$
R6	$2CH_3 \leftrightarrow C_2H_5 + H$	$6.84x10^{12}$	0.10	$4.435x10^4$
R7	$CH_2 + H_2 \leftrightarrow CH_3 + H$	$5.00x10^5$	2.00	$3.025x10^4$
R8	$2CH_2 \leftrightarrow C_2H_2 + H_2$	$1.60x10^{15}$	0	$4.997x10^4$
R9	$C_2H_4 + H_2 \leftrightarrow C_2H_2 + H_2 + H_2$	$1.58x10^{51}$	-9.30	$4.092x10^5$
R10	$C_2H_6 + H \leftrightarrow C_2H_5 + H_2$	$1.15x10^8$	1.90	$3.151x10^4$
R11	$2CH_3 + H_2 \leftrightarrow C_2H_6 + H_2$	$3.40x10^{37}$	-7.03	$1.156x10^4$
R12	$CH + H \leftrightarrow C + H_2$	$1.65x10^{14}$	0	0
R13	$CH + H_2 \leftrightarrow CH_2 + H$	$1.08x10^{14}$	0	$1.301x10^4$
R14	$2CH_2 \leftrightarrow C_2H_2 + 2H$	$2.00x10^{14}$	0	$4.598x10^4$
R15	$C + CH_2 \leftrightarrow C_2H + H$	$5.00x10^{13}$	0	0
R16	$CH + CH_2 \leftrightarrow C_2H_2 + H$	$4.00x10^{13}$	0	0
R17	$CH_2 + H + H_2 \leftrightarrow CH_3 + H_2$	$1.04x10^{26}$	-2.76	$6.693x10^3$
R18	$CH + H_2 + H_2 \leftrightarrow CH_3 + H_2$	$4.82x10^{25}$	-2.80	$2.469x10^3$

species density profiles reported in the literature, particularly for the key growth species H and CH_3 near the substrate surface, based on a comparison with F. Silva et. al. [20]. This comparison was done using a similar geometry to F. Silva. et. al. A comparison for H and CH_3 are shown in Appendix B.

The set of equations are solved using the finite element method in COMSOL Multiphysics [30]. A detailed report of the simulation setup in COMSOL can be found in Princeton University Library's Master's Thesis Collection [31]. This report was generated using COMSOL's report generator tool. The mesh is shown in Figure 2 and consists of 24,919 domain elements and 1,413 boundary elements. The maximum element size at the substrate is 160 μm, at all other boundaries is 1 mm, and for the remainder of the domain is 2 mm. The total number of degrees of freedom solved for is 654,201, plus 34,597 internal degrees of freedom. Simulations were performed in a Dell Inspiron 7706 2-in-1 laptop, with typical run times ranging from two to three hours.

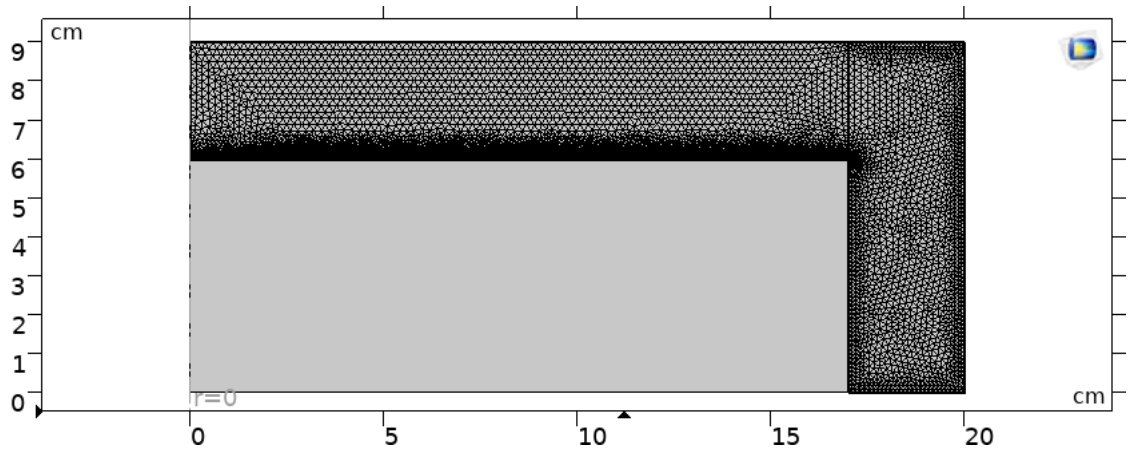

Figure 2: Simulation mesh for two-dimensional cylindrical model.

3 Results and discussion

3.1 Base simulation

The model was run with base case conditions of a nonuniform temperature profile, 200 torr pressure, 6.5 standard liters per minute (lpm) inlet flow rate, 136 kW of total power applied, uniform CH_4 mole fraction of 4% at the inlet, and a 3 cm gap between the substrate and inlet. The nonuniform power application and resulting temperature profile are shown in Figures 3 and 4. The resulting mole fractions of H, H_2, CH_3, CH_4, and C_2H_2 are shown in Figures 5-9. The mole fractions of all other species are included in Appendix C. Streamlines for the velocity are shown in Figure 10.

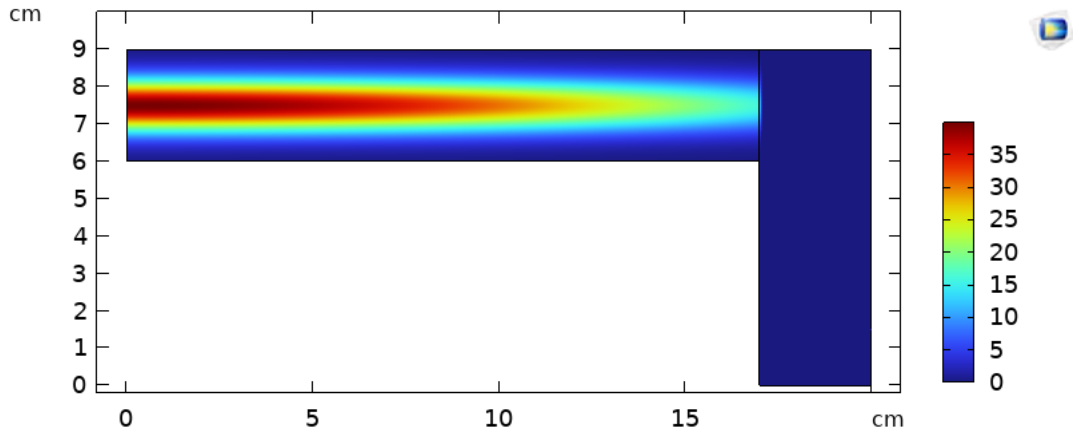

Figure 3: Nonuniform power deposition for base case simulation ($\frac{\text{W}}{\text{cm}^3}$).

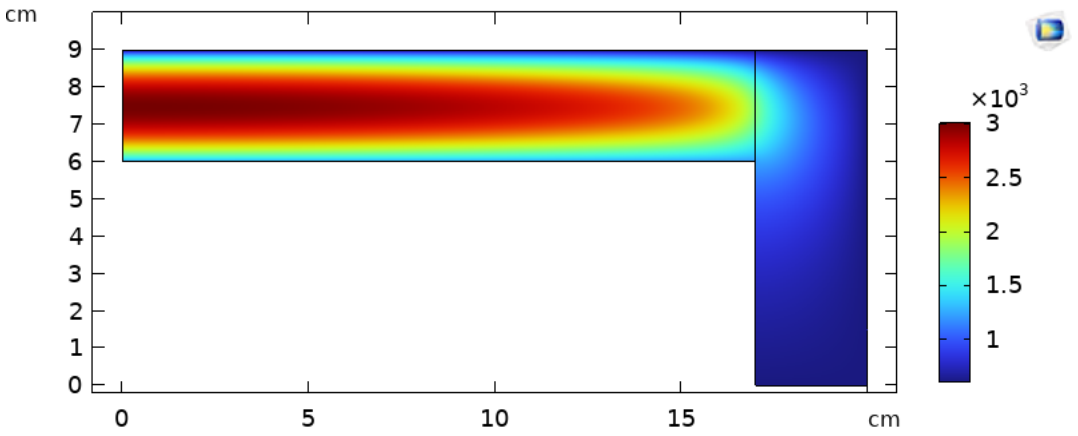

Figure 4: Resulting temperature profile from nonuniform power deposition for base case simulation (K).

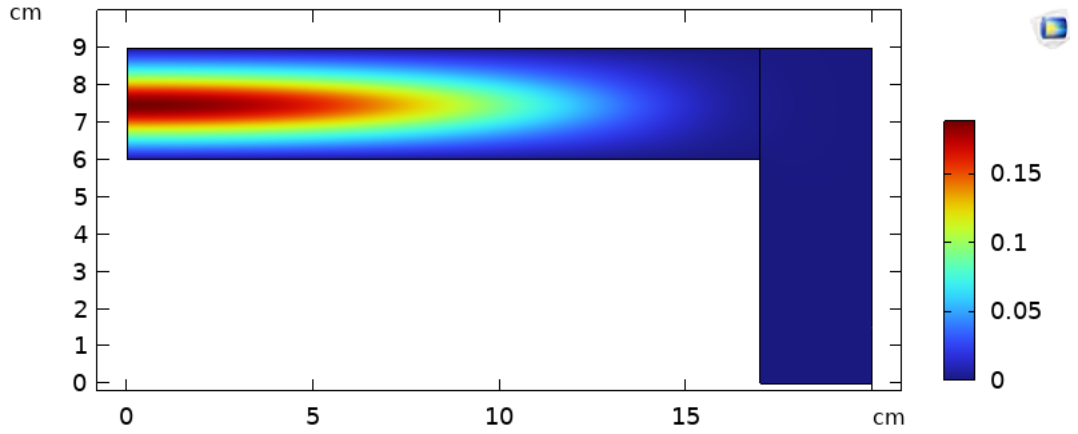

Figure 5: Mole fraction of H for base case simulation.

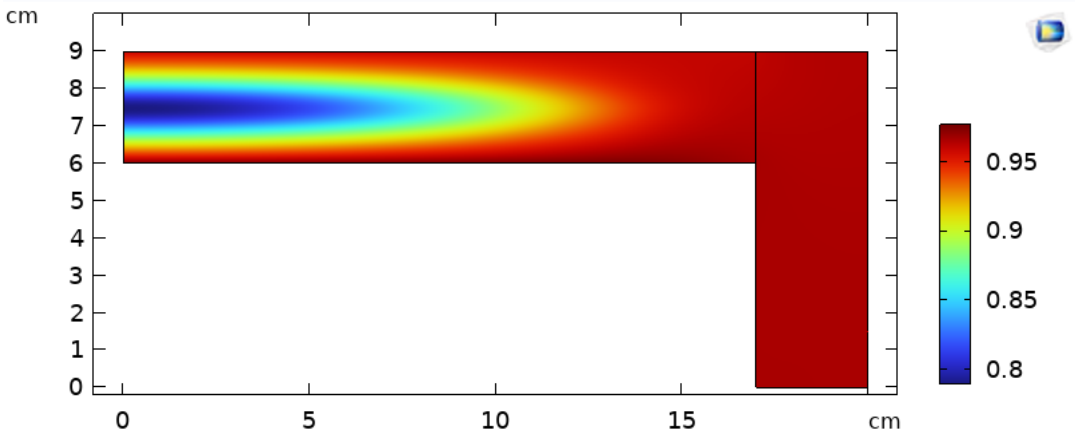

Figure 6: Mole fraction of H_2 for base case simulation.

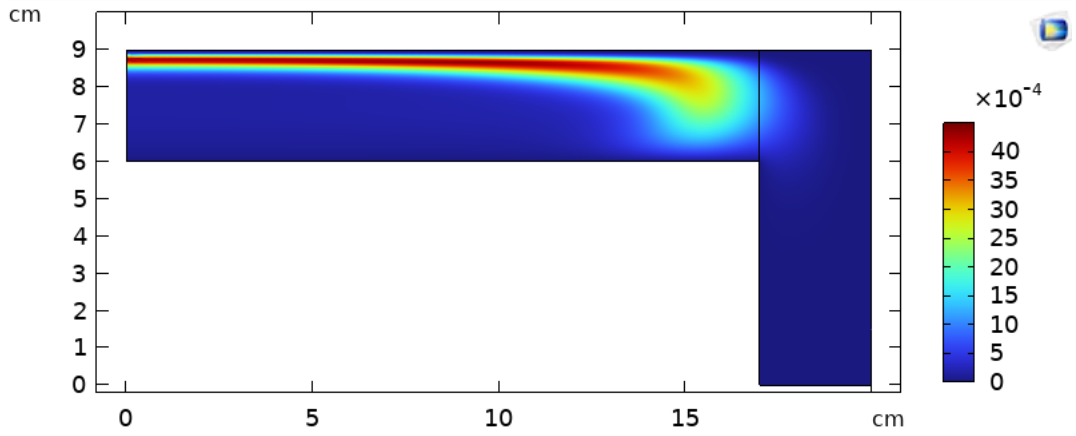

Figure 7: Mole fraction of CH_3 for base case simulation.

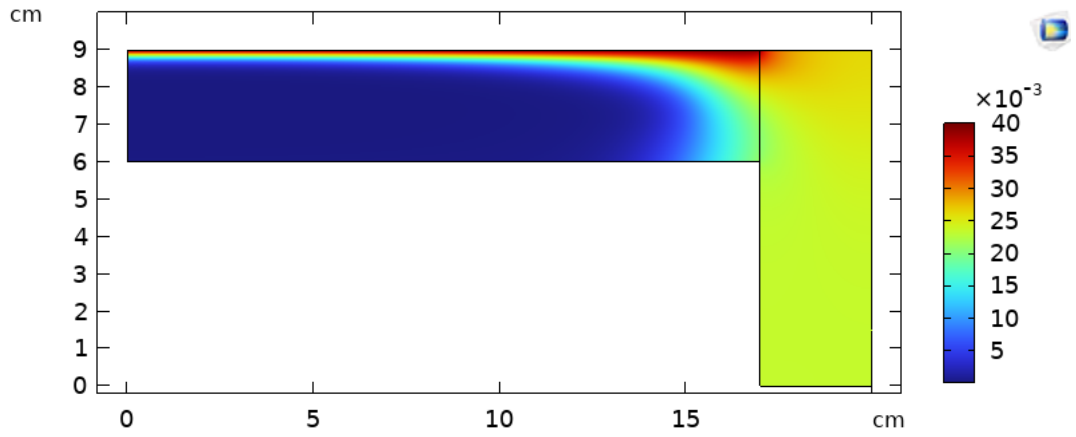

Figure 8: Mole fraction of CH_4 for base case simulation.

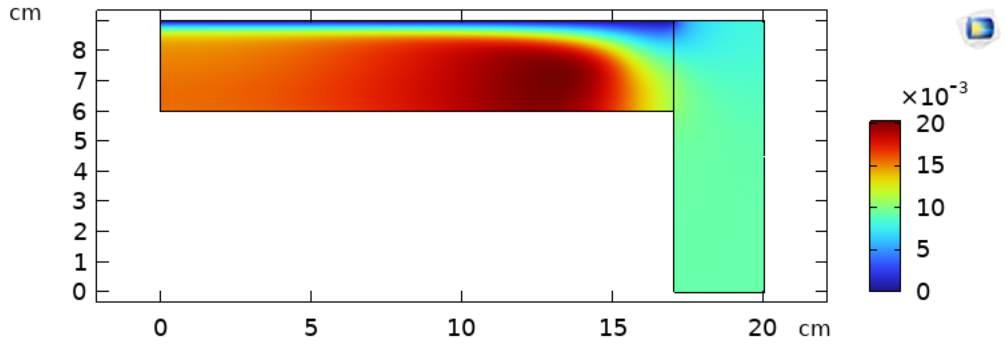

Figure 9: Mole fraction of C_2H_2 for base case simulation.

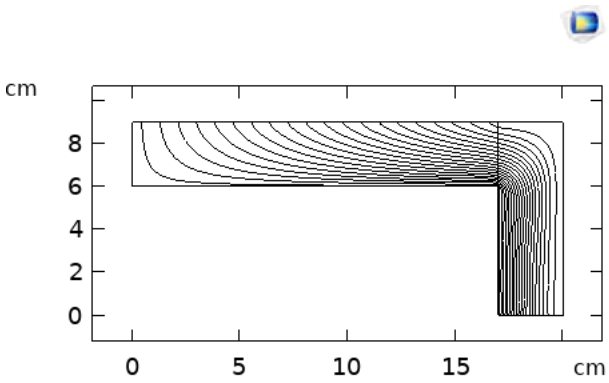

Figure 10: Velocity streamlines for base case simulation.

To assess the extent to which the species distributions deviate from equilibrium, the mole fractions of H, H_2, CH_3, and CH_4 from the model are compared to their corresponding equilibrium values at the local gas temperature. Figures 11 and 12 present the mole fractions of H and H_2 as a function of the axial coordinate z along the centerline, with the equilibrium values calculated assuming instantaneous equilibration at each position. According to Figure 11, H is not in equilibrium. At its peak value, the model predicts that H is present in a smaller amount than equilibrium predicts. Because of its small weight, H diffuses away rapidly at high temperatures, leading to its model-predicted mole fraction being lower than equilibrium predictions in the high-temperature zone and higher than equilibrium predictions in the low-temperature zones. This is supported by Damkohler numbers being less than 1 for the dominant reactions forming H, reactions R1 and R3, indicating that diffusion dominates reactions. H_2 shows the opposite trend; in the high-temperature zone, the model predicts H_2 to be at a higher mole fraction than predicted by equilibrium. With

less H present, the equilibrium of H_2 dissociation and recombination cannot be maintained, leading to lower dissociation of H_2 in the high temperature zone. In contrast, with more H present in the low-temperature zones, H_2 dissociation proceeds more rapidly, leading to lower mole fractions than predicted by equilibrium.

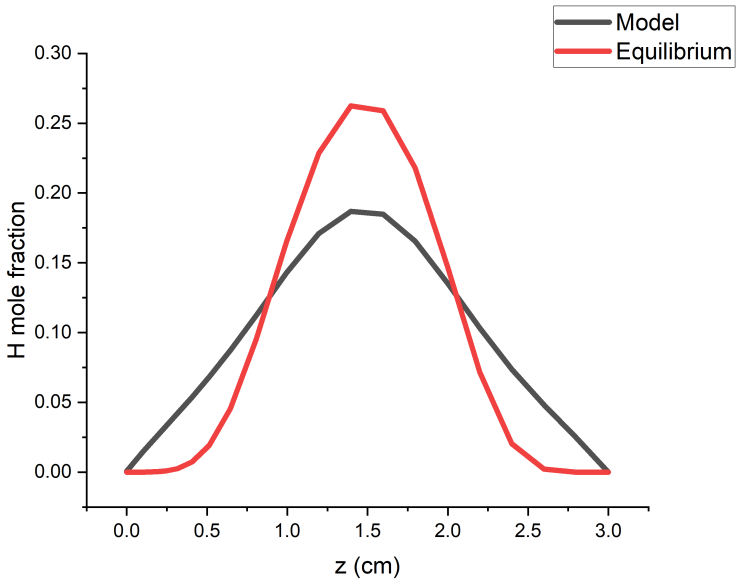

Figure 11: Comparison of the mole fraction of H from the model and equilibrium as a function of the axial coordinate z.

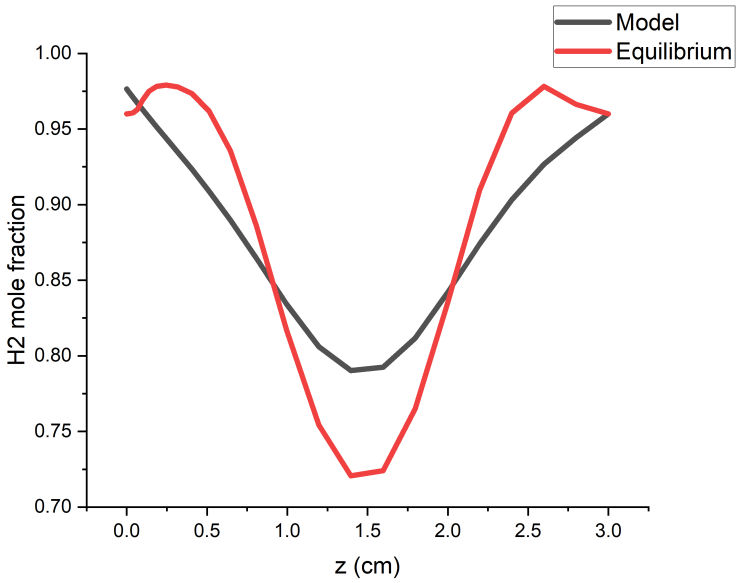

Figure 12: Comparison of the mole fraction of H_2 from the model and equilibrium as a function of the axial coordinate z.

Figures 13 and 14 compare the mole fractions of CH_3 and CH_4 predicted from the model, equilibrium, and from Equations 12 and 13, where the rate constants refer to the reactions in Table 1. Prior work by Ashfold and Mankelevich derived a similar expression to Equation 12, where we have simplified it based on the dominant terms in the expression [32]. Equation 13 is Equation 12 rearranged for $[CH_4]$. These expressions were converted to mole fractions in Figures 13 and 14 using the total particle density. According to Figures 13 and 14, although the comparisons show that CH_3 and CH_4 deviate from their predicted equilibrium values, they are in fact in equilibrium according to Equations 12 and 13 which can be seen by the model and equation lines overlapping. This deviation is a consequence of H not being in equilibrium, which CH_3 and CH_4 both depend on. The model predicts that CH_3 is higher than equilibrium values due to H being higher than equilibrium values. With more H present near the inlet, the dissociation of CH_4 is increased beyond what equilibrium predicts, leading to higher amounts of CH_3. The peak in CH_3 mole fraction corresponds to the location where the temperature is near 1600 K, where CH_3 production is maximized. The equilibrium of CH_3 and CH_4 is supported by their high Damkohler numbers, indicating that these species rapidly equilibrate before they can diffuse. These species remain in

equilibrium throughout the reactor except for very close to the substrate, as illustrated in Figures 15 and 16.

$$[CH3] = \frac{k_4[H][CH_4]}{[H_2] + (k_{-4} + k_5[H])} \tag{12}$$

$$[CH4] = \frac{[CH_3]([H_2] + (k_{-4} + k_5[H]))}{k_4[H]} \tag{13}$$

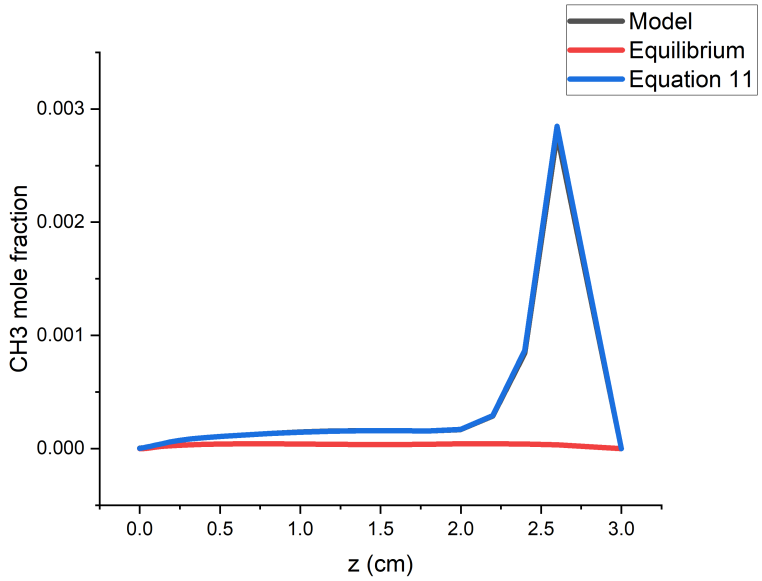

Figure 13: Comparison of the mole fraction of CH_3 from the model, equilibrium, and Equation 12 as a function of the axial coordinate z.

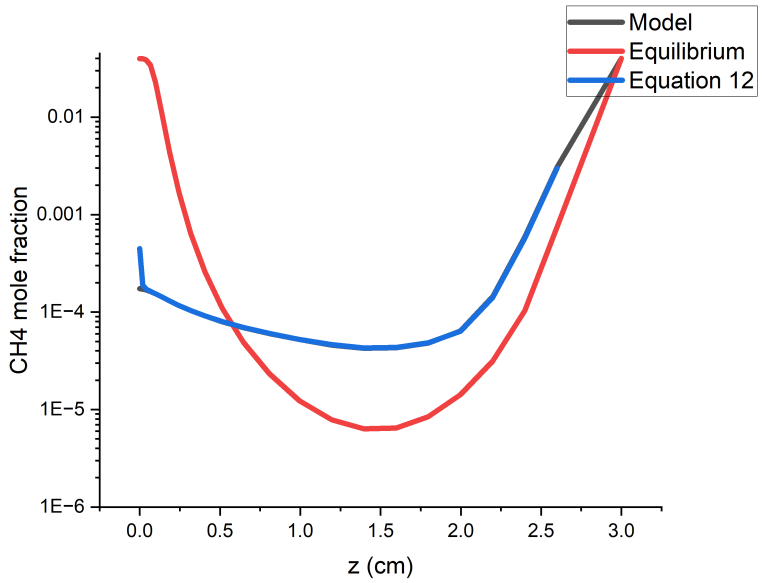

Figure 14: Comparison of the mole fraction of CH_4 from the model, equilibrium, and Equation 12 as a function of the axial coordinate z.

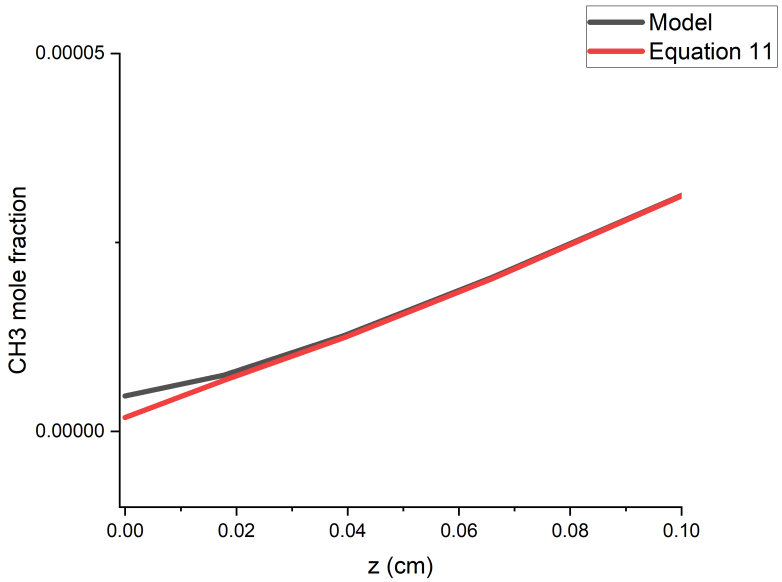

Figure 15: Comparison of the mole fraction of CH_3 from the model and Equation 12 as a function of the axial coordinate z within 1 mm of the substrate.

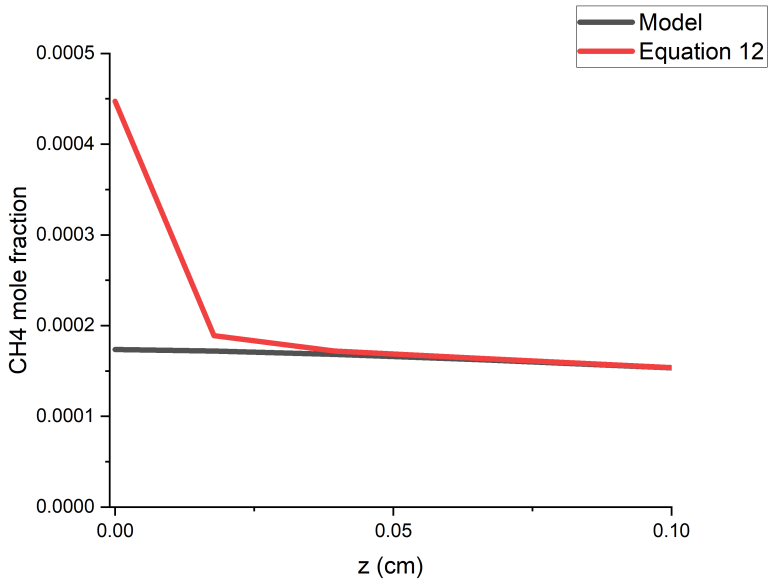

Figure 16: Comparison of the mole fraction of CH_4 from the model and Equation 13 as a function of the axial coordinate z within 1 mm of the substrate.

While Figures 11 and 13 appear to show the H and CH_3 mole fractions equivalent to the equilibrium predictions on a linear scale, on a log scale very near the substrate it is clear that they are different. Figures 17 and 18 show that at the substrate, the model predicts the mole fraction of H to be three orders of magnitude higher than equilibrium predicts, and the mole fraction of CH_3 to be one order of magnitude higher than equilibrium predicts.

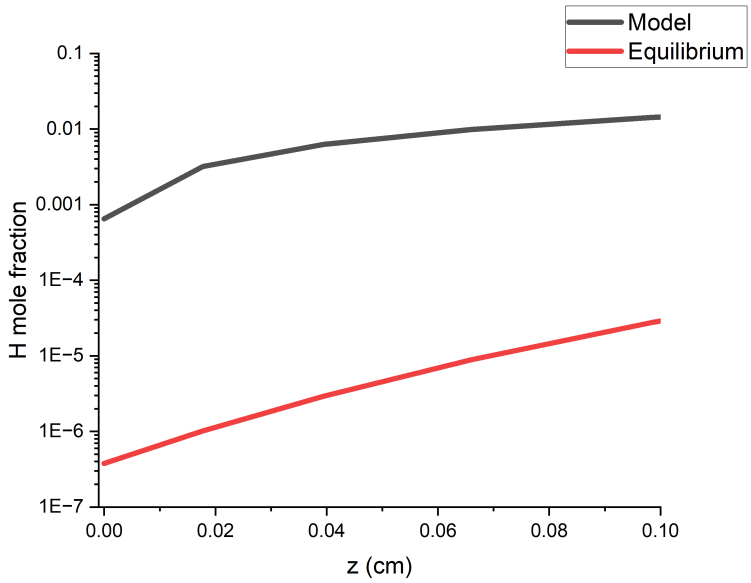

Figure 17: Comparison of the mole fraction of H from the model and equilibrium as a function of the axial coordinate z very close to the substrate.

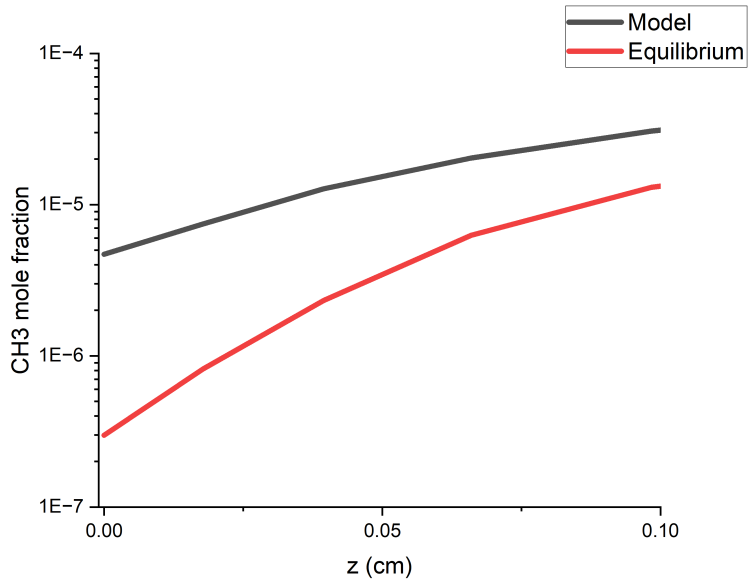

Figure 18: Comparison of the mole fraction of CH_3 from the model and equilibrium as a function of the axial coordinate z.

The equilibrium mole fraction for each species in the model is also shown as a function of temperature at 200 torr in Figure 19.

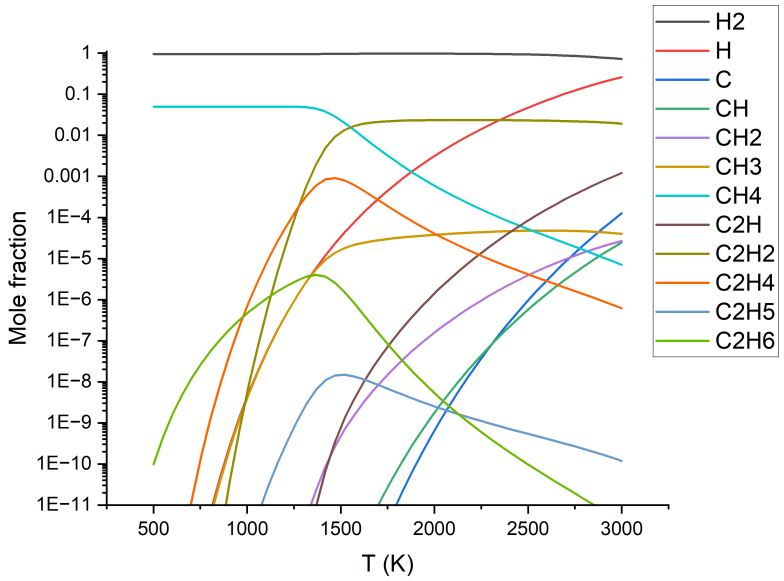

Figure 19: Equilibrium mole fractions as a function of temperature at 200 torr.

The growth rate, defect ratio, and concentrations of H and CH_3 were calculated 100 μm from the substrate surface and are shown in Figures 20-23. The growth rate was calculated according to Equation 8. The defect ratio is proportional to $\frac{G}{[H]^2}$, as proposed by Goodwin [22]. The defect ratio was scaled to unity such that the ratio is equal to 1 at the centerline for the base case simulation. Figures 20-23 show that at the base conditions, the growth rate and defects are highly nonuniform. Based on Equation 8, this is due to the nonuniformity of H and CH_3. In order to improve the uniformity and magnitude of the growth rate and defects, it is therefore necessary to improve the uniformity and magnitude of the concentrations of H and CH_3.

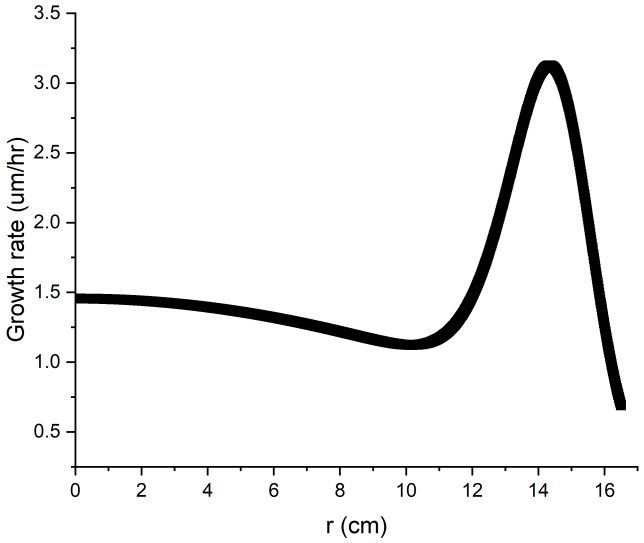

Figure 20: Radial growth rate profile near substrate surface for base case simulation.

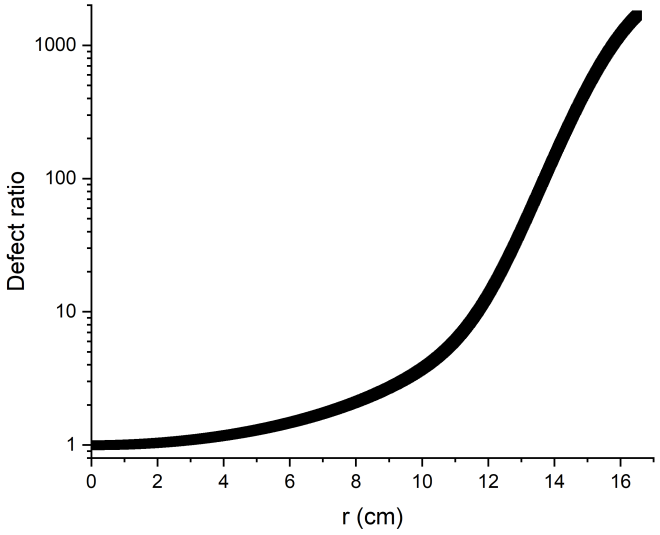

Figure 21: Radial defect ratio profile near substrate surface for base case simulation.

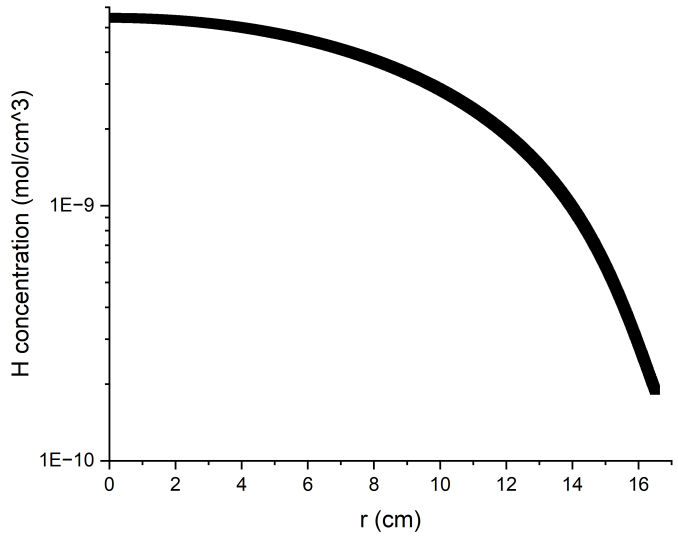

Figure 22: Radial H concentration profile near substrate surface for base case simulation.

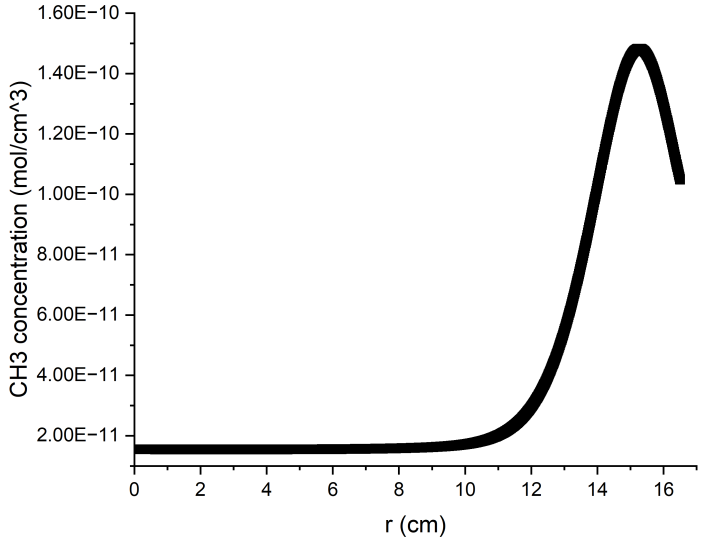

Figure 23: Radial CH_3 concentration profile near substrate surface for base case simulation.

3.2 Effects of altering pressure, power magnitude, and gap size

Changing the pressure, power magnitude, and gap size between the substrate and the inlet primarily affect the magnitude of the growth rate and defect ratio. Each of these parameters were

varied individually while maintaining all other base case conditions.

Reducing the pressure from 200 torr to 100 torr increases the growth rate from approximately 1.45 to 1.55 $\frac{\mu m}{hr}$ at the centerline and from approximately 3.12 to 4.21 $\frac{\mu m}{hr}$ at the maximum. The maximum growth rate shifts radially from 14.3 to 12.6 cm. This increase is driven by enhanced diffusion at lower pressures, which allows CH_3 to more effectively reach the substrate, while the highly diffuse H atoms spread out more rapidly, loading to a local decrease in H concentration near the substrate. Consequently, the scaled defect ratio increases from 1 to 2.2 at the centerline.

Raising the applied power from 136 to 150 kW increases the growth rate from 1.45 to 1.62 $\frac{\mu m}{hr}$ at the centerline, and from 3.12 to 3.15 $\frac{\mu m}{hr}$ at the maximum. The maximum growth rate shifts radially from 14.3 to 14.9 cm. The CH_3 concentration decreases beyond approximately 6 cm radially, while the H concentration is consistently higher throughout the near-substrate region. This trend is caused a decrease in the diffusion of CH_3 near the substrate, while H has an increase in diffusion near the substrate. The magnitude of the scaled defect ratio decreases from 1 to 0.7 at the centerline.

Expanding the gap from 3 to 4 cm while maintaining the magnitude and location of power applied decreases the growth rate from 1.45 to 1.38 $\frac{\mu m}{hr}$ at the centerline, and from 3.12 to 1.04 $\frac{\mu m}{hr}$ at the maximum. The maximum growth rate shifts radially from 14.3 to 14.9 cm. The CH_3 concentration decreases throughout the near-substrate region, while the H concentration decreases near the centerline, but increases after 6.5 cm radially. With a larger gap, the reactor temperature is higher far from the substrate than in the base case. This causes CH_3 to diffuse away or be consumed before it can reach the substrate. The magnitude of the scaled defect ratio remains the same near the centerline, but decreases after 4.5 cm radially. Decreasing the gap from 3 to 2 cm, however, showed improved results in the growth rate. The maximum power deposition was shifted to 7 cm axially, and was set to maintain the same maximum temperature of 3000 K. The growth rate increases from 1.45 to 2.85 $\frac{\mu m}{hr}$ at the centerline, and from 3.12 to 8.78 $\frac{\mu m}{hr}$ at the maximum. The maximum growth rate shifts radially from 14.3 to 13.1 cm. The magnitude of the scaled defect ratio remains the same near the centerline, but begins to increase after about 4 cm radially.

3.3 Effect of improving power uniformity

While maintaining all other base case conditions, the power deposition was made more uniform according to Figure 24, resulting in the temperature profile shown in Figure 25. The radial profiles of the growth rate, defect ratio, and concentrations of H and CH_3 are shown in Figures 26-29. As the uniformity of the temperature profile is improved, the radial concentrations of CH_3 and H become more uniform, which in turn results in a more uniform growth rate. This highlights the strong dependence of species transport and reaction kinetics on temperature. In practice, achieving a more uniform power deposition may not be feasible. Therefore, we explore alternative conditions that could improve the uniformity of diamond deposition.

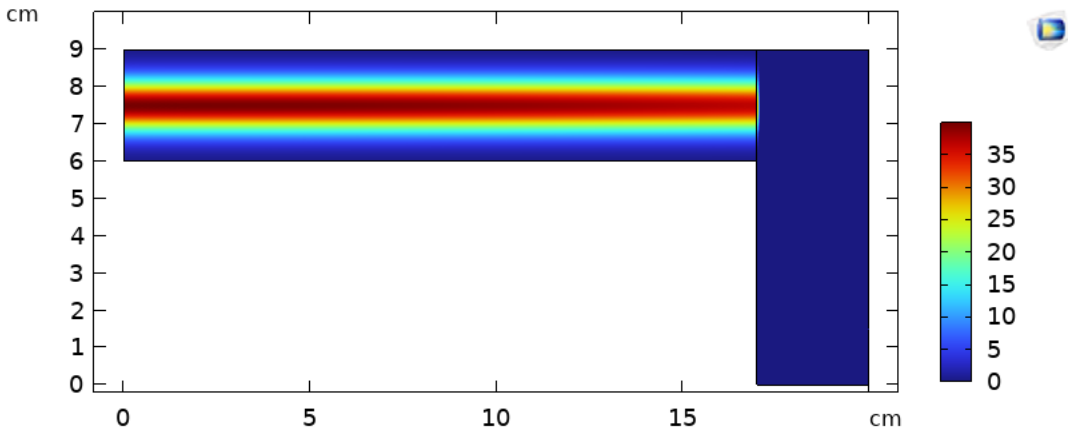

Figure 24: Uniform power deposition profile.

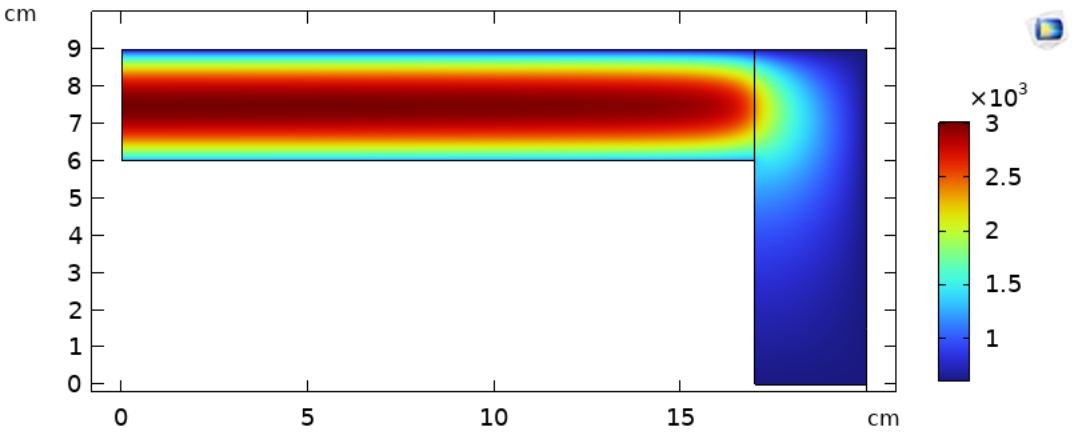

Figure 25: Uniform temperature deposition profile.

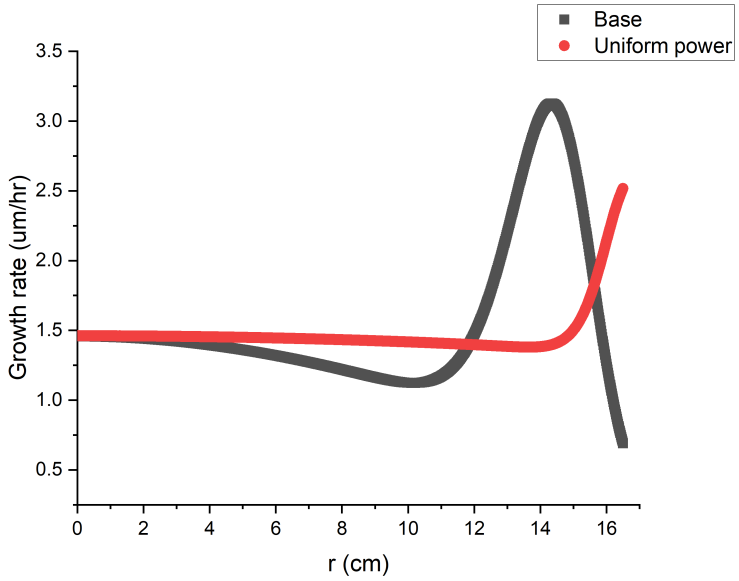

Figure 26: Radial growth rate profile near substrate surface for uniform power simulation.

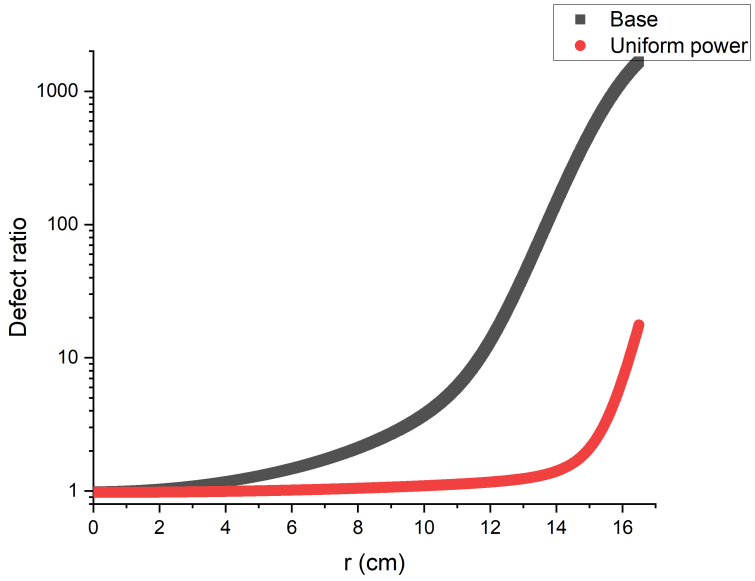

Figure 27: Radial defect ratio profile near substrate surface for uniform power simulation.

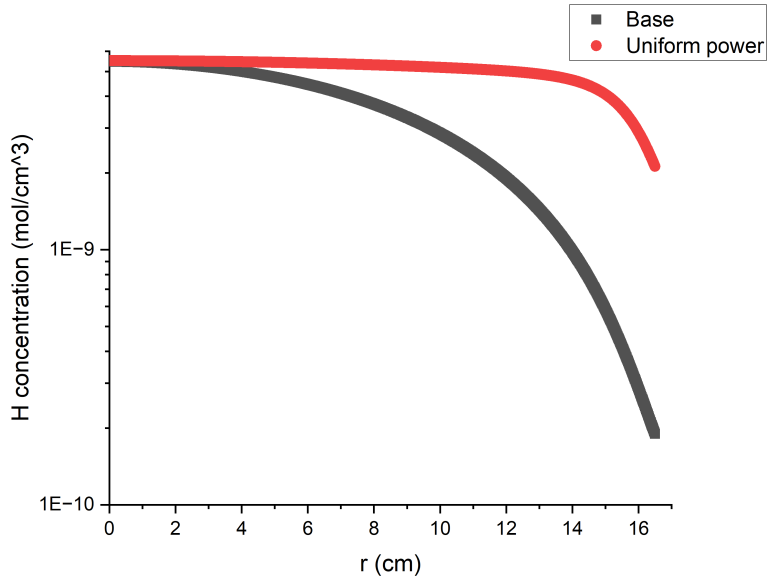

Figure 28: Radial H concentration profile near substrate surface for uniform power simulation.

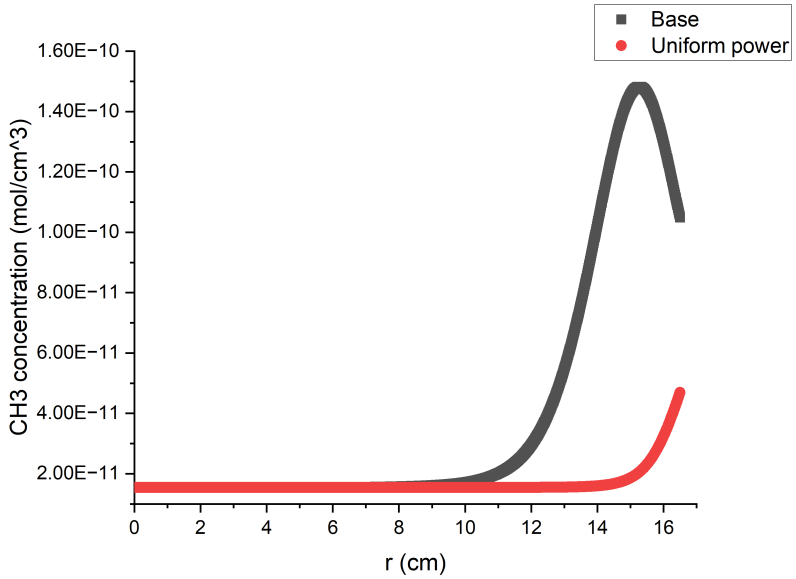

Figure 29: Radial CH_3 concentration profile near substrate surface for uniform power simulation.

3.4 Effect of increasing inlet flow rate

The inlet flow rate was increased from 6.5 lpm to 130 lpm while maintaining all other base case conditions. The radial profiles of the growth rate, defect ratio, and concentrations of H,

and CH_3 are shown in Figures 30-33. Increasing the inlet flow rate shifts the temperature profile outward radially, which in turn causes the CH_3 and H concentrations to move outward as well. The growth rate follows the same trend, becoming more uniform as its profile shifts outward radially. The magnitude of the growth rate increases near the centerline due to the higher Peclet number associated with increased flow, which enhances the transport of CH_3 and H toward the substrate surface. The higher and more uniform H concentration at elevated flow rates also leads to a lower and more uniform defect ratio. Lower CH_3 concentrations in the peak region near 15 cm lead to lower growth rates in this region, leading to a much more uniform profile.

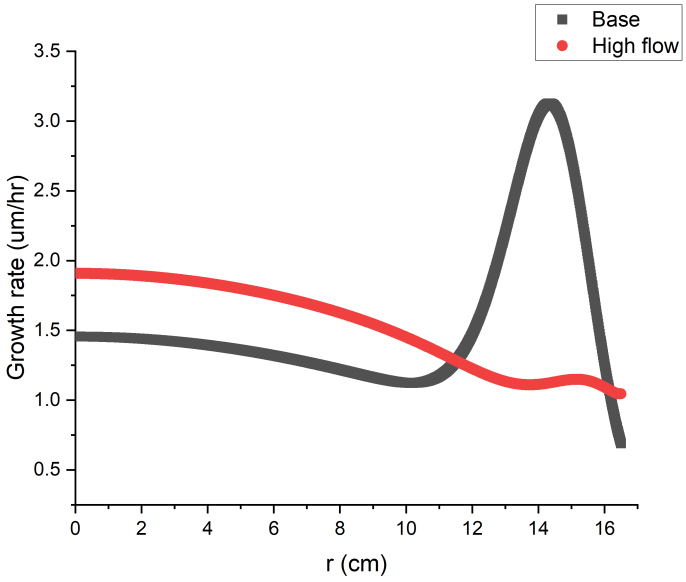

Figure 30: Radial growth rate profile near substrate surface for high flow simulation.

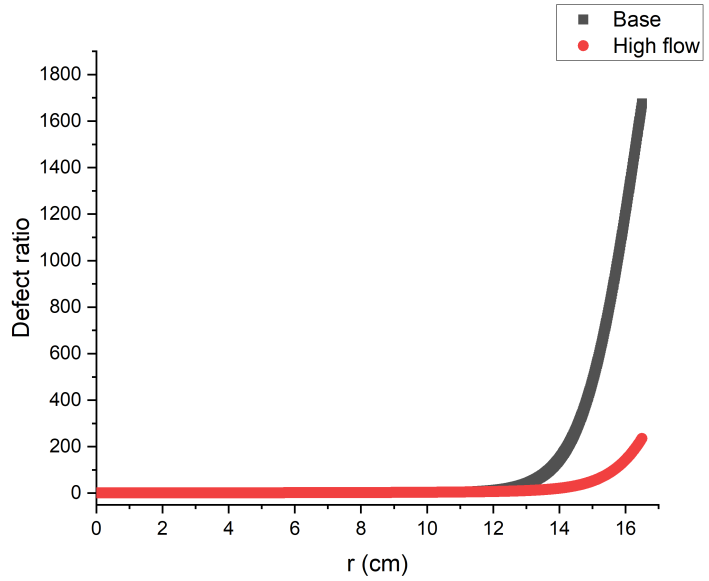

Figure 31: Radial defect ratio profile near substrate surface for high flow simulation.

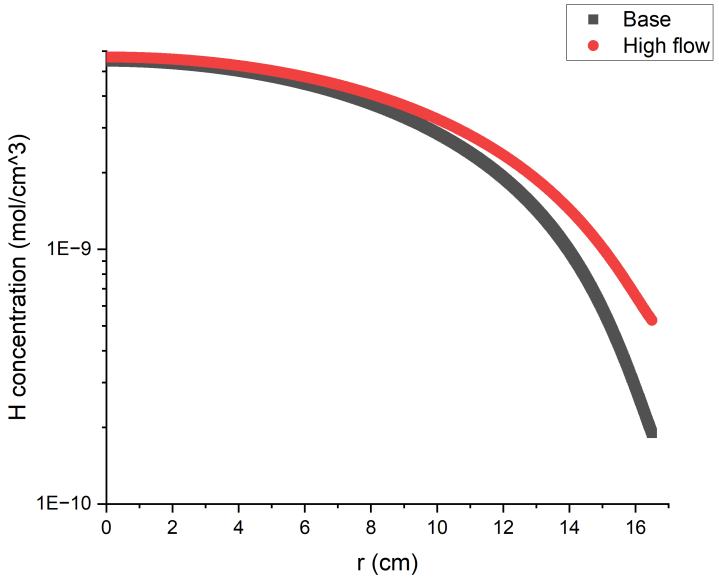

Figure 32: Radial H concentration profile near substrate surface for high flow simulation.

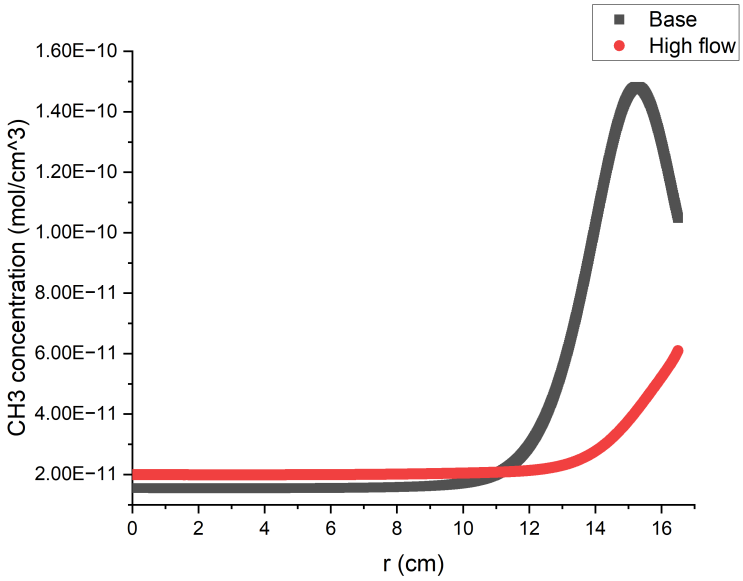

Figure 33: Radial CH_3 concentration profile near substrate surface for high flow simulation.

3.5 Effect of altering CH_4 concentration profile at the inlet

While maintaining all other base case conditions, the CH_4 mole fraction at the inlet was altered from a uniform profile to a nonuniform profile. The nonuniform profile includes a step change from 4% to 12% at 8 cm radially and from 12% to 1.8% at 13 cm radially. The radial profiles of the growth rate, defect ratio, and concentrations of H and CH_3 are shown in Figures 34-37. The results show that by changing the uniformity of the CH_4 inlet mole fraction, the uniformity of the CH_3 concentration near the substrate can be dramatically improved, resulting in a more uniform growth rate. Because the H concentration remains unchanged near the substrate, the defect ratio does not have much alteration.

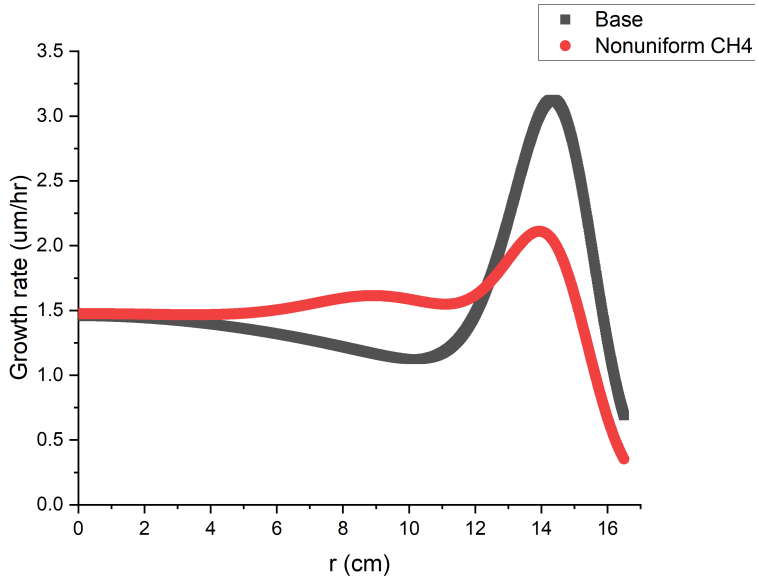

Figure 34: Radial growth rate profile near substrate surface for nonuniform CH_4 inlet mole fraction simulation.

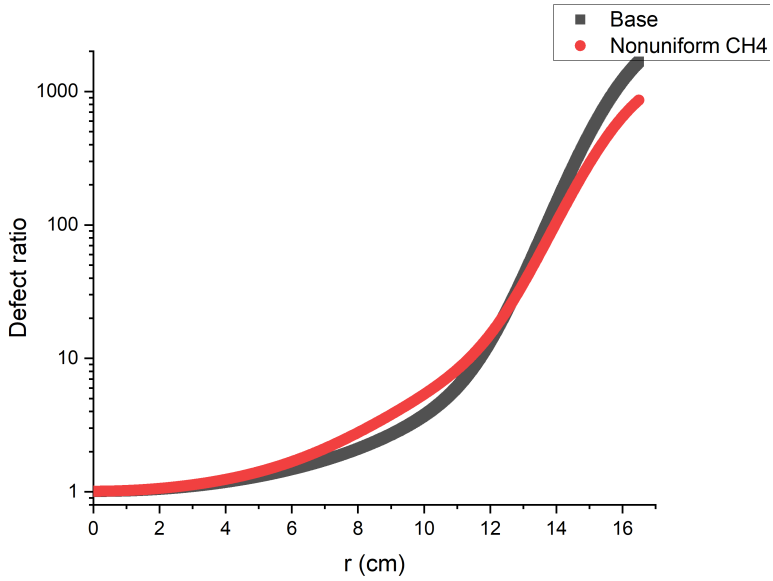

Figure 35: Radial defect ratio profile near substrate surface for nonuniform CH_4 inlet mole fraction simulation.

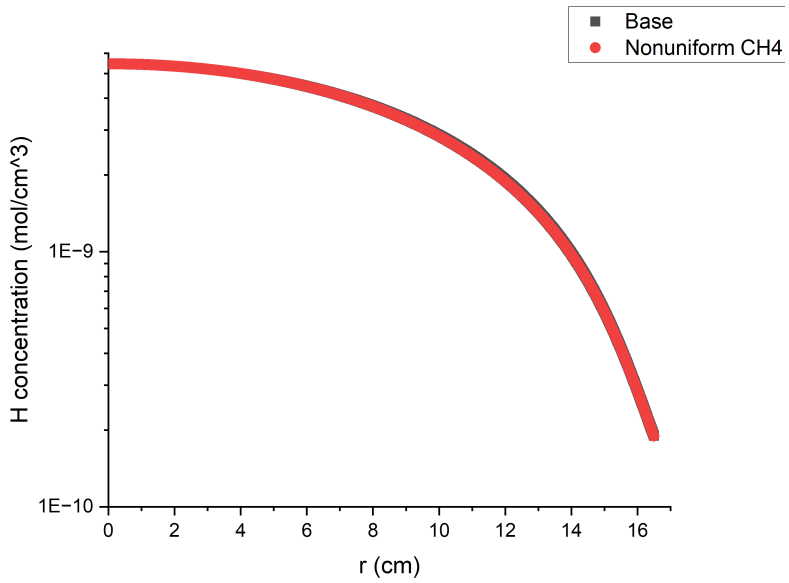

Figure 36: Radial H concentration profile near substrate surface for nonuniform CH_4 inlet mole fraction simulation.

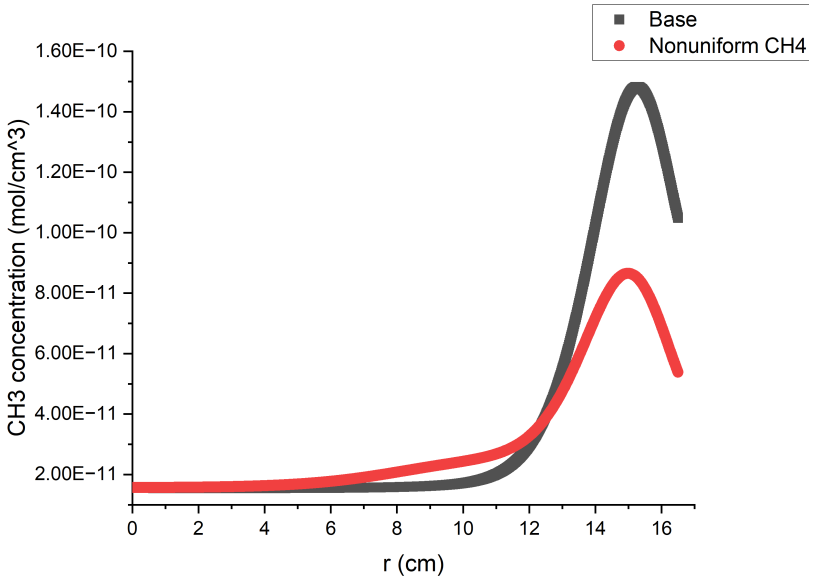

Figure 37: Radial CH_3 concentration profile near substrate surface for nonuniform CH_4 inlet mole fraction simulation.

3.6 Effect of decreasing the maximum temperature

Generating a plasma with a maximum temperature of 3000 K may be difficult in practice. This section explores the possibility of generating a plasma with a maximum temperature of 2000 K. While maintaining all other base case conditions, the applied power was decreased to 41 kW such that the maximum temperature was near 2000 K. The radial profiles of the growth rate, defect ratio, and concentrations of H and CH_3 are shown in Figures 38-41. The results show that the H and CH_3 concentrations drop by several orders of magnitude, leading to a dramatically lower growth rate and higher defect ratio. While achieving a plasma with this power may be more feasible, the results are not sufficient for diamond growth.

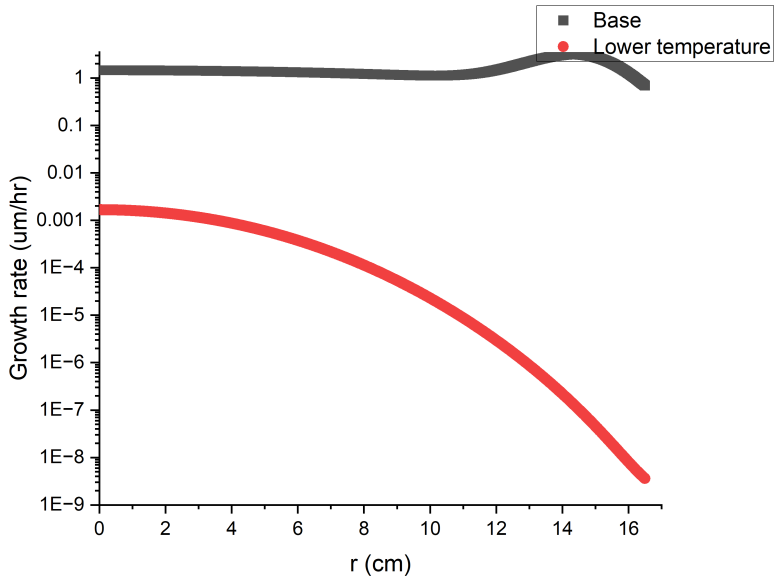

Figure 38: Radial growth rate profile near substrate surface for lower maximum temperature simulation.

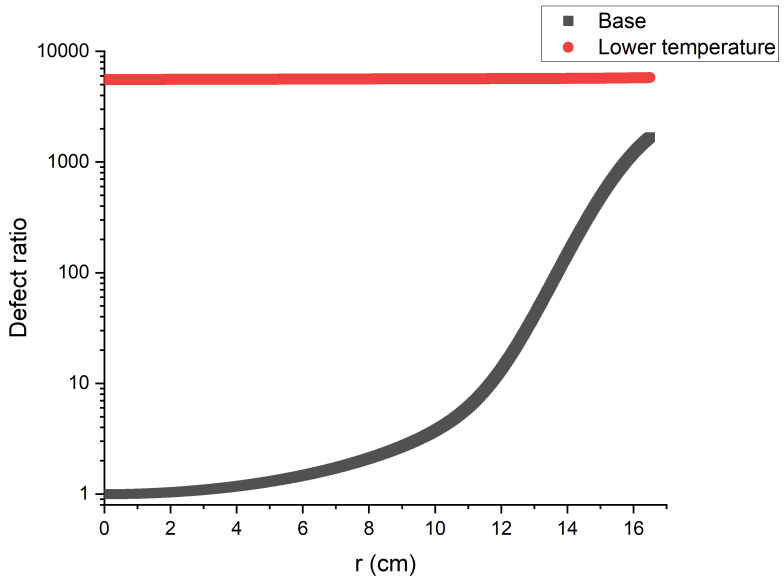

Figure 39: Radial defect ratio profile near substrate surface for lower maximum temperature simulation.

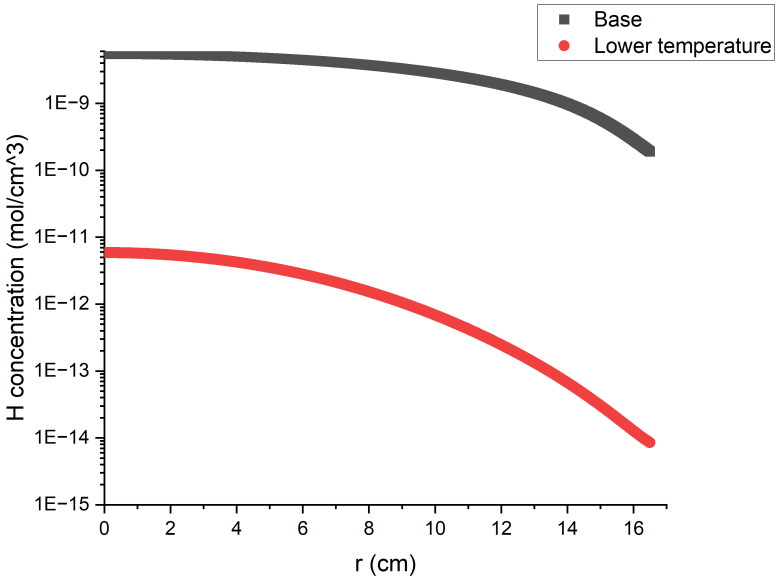

Figure 40: Radial H concentration profile near substrate surface for lower maximum temperature simulation.

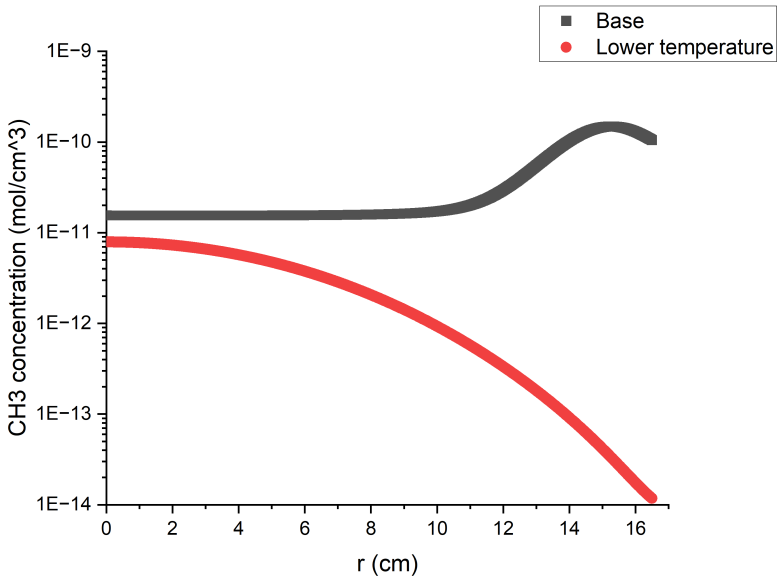

Figure 41: Radial CH_3 concentration profile near substrate surface for lower maximum temperature simulation.

3.7 Processing efficiency compared to MPCVD reactor

Processing efficiencies were compared between this work's base case parallel plate configuration and Butler's MPCVD reactor [16]. For constistent comparisons, the simulation was run at 150 torr. The maximum growth rate in the MPCVD reactor was 4.5 $\frac{\mu m}{hr}$ across a 3 cm diameter substrate, resulting in 3.18x10^{-3} $\frac{cm^3}{hr}$ volumes of diamond grown. This work had an average growth rate in the base case simulation of 2.4 $\frac{\mu m}{hr}$ across a 30 cm diameter substrate, resulting in 0.167 $\frac{cm^3}{hr}$ volumes of diamond grown. The MPCVD reactor applied a total power of 1.5 kW and 25 sccm of CH_4, while this work applied a total power of 136 kW and 260 sccm of CH_4. With these values, the MPCVD has a growth per unit power of 2.12x10^{-3} $\frac{cm^3}{hr \cdot kW}$ and a growth per unit CH_4 of 1.27x10^{-4} $\frac{cm^3}{hr \cdot sccm}$, while the parallel plate configuration has a growth per unit power of 1.23x10^{-3} $\frac{cm^3}{hr \cdot kW}$ and a growth per unit CH_4 of 6.41x10^{-4} $\frac{cm^3}{hr \cdot sccm}$ In summary, the MPCVD reactor is 1.7x more efficient in terms of power used, but the parallel plate configuration is 5.1x more efficient in terms of CH_4 used.

3.8 Comparison of chemical species results and growth rates to MPCVD reactor

Number densities of H and CH_3 were compared to Butler by multiplying mole fractions by the total particle density using the 150 torr simulation [16]. In the parallel plate configuration, the peak H number density is 6.50x10^{16} cm^{-3} compared with 4.03x10^{16} cm^{-3} in the MPCVD reactor. Near the substrate, the parallel plate configuration has a H number density of 1.20x10^{15} cm^{-3}, while in the microwave reactor it is near 1.86x10^{16} cm^{-3}. The number density of H decreases to zero by the end of the substrate in the parallel plate configuration, while in the MPCVD reactor the number density remains high throughout the substrate region. The CH_3 number density peaks at 4.22x10^{15} cm^{-3} in the parallel plate configuration, while it peaks at 3.92x10^{14} cm^{-3} in the MPCVD reactor. However, the peak in the MPCVD reactor is next to the substrate, while in the parallel plate configuration it is located near the reactor inlet. At a similar location, the MPCVD reactor has a CH_3 number density near 2.1x10^{14} cm^{-3}. The MPCVD reactor is characterized as having a hemispherical shell of CH_3 that peaks next to the substrate, while the parallel plate configuration sees its peak close to the reactor inlet and decreases as it moves down the reactor. It is important to note the difference in temperature profiles between the two reactors. The MPCVD reactor has high temperatures next to the substrate, while in the parallel plate reactor, high temperatures are strictly 1.5 cm above the substrate. With a similar temperature profile as the MPCVD reactor, the parallel plate reactor would likely similarly have a significant amount of CH_3 next to the substrate. Above the substrate, the parallel plate configuration has a CH_3 number density of 1.20x10^{13} cm^{-3} at the centerline of the reactor, while in the MPCVD reactor it is near 1.81x10^{14} cm^{-3}. Because the MPCVD reactor has higher number densities of H and CH_3 near the substrate, it is expected that the MPCVD reactor will yield higher growth rates according to Goodwin's growth rate expression [22].

In the MPCVD reactor, growth rates can be approximated as

$$G[\mu\mathrm{m}\cdot\mathrm{h}^{-1}] \leq 0.15\mathrm{x}p[\mathrm{Torr}]X_0^{0.5} \tag{14}$$

where X_0 is the inlet CH_4 mole fraction. To evaluate whether growth rates in the parallel plate configuration follow the trends in pressure and inlet CH_4 mole fraction, simulations were run with base conditions at pressures of 150 and 100 torr, and with base conditions at 6% and 8% inlet mole fractions of CH_4. Comparisons of growth rates from these simulations are presented in Figures 42 and 43. Equation 14 predicts that the growth rate should scale linearly with pressure and as a square root with inlet CH_4 mole fraction. However, Figures 42 and 43 show that this is not the case in the parallel plate configuration. While the growth rate increases when varying pressure from 200 to 150 torr, it decreases when varying pressure from 150 to 100 torr. Additionally, while the growth rate increases when varying the methane inlet mole fraction from 4% to 6%, it remains the same when varying from 6% to 8%. Therefore, Equation 14 is not appropriate for estimating growth rates in the parallel plate configuration.

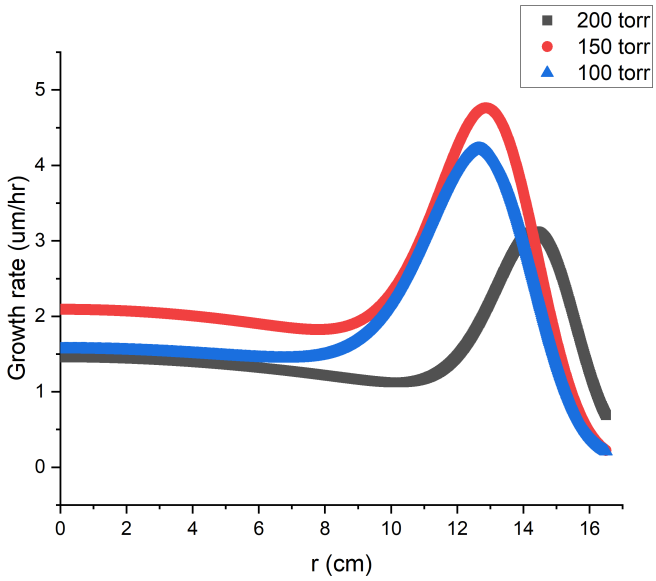

Figure 42: Radial growth rate profile near substrate surface for varying pressures.

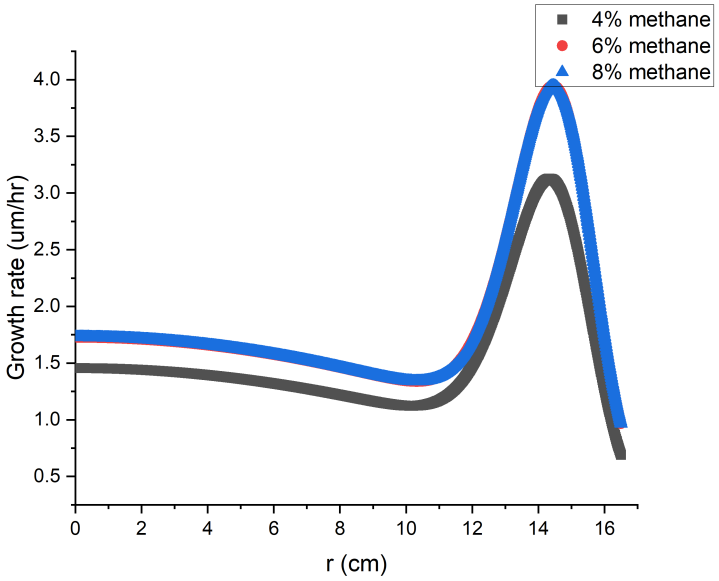

Figure 43: Radial growth rate profile near substrate surface for varying methane inlet mole fractions.

3.9 Heat flow to the substrate

Optimal diamond growth is known to occur at temperatures near 1200 K. In the model, this is set as a Dirichlet boundary condition. In practice, there is a heat flux to the substrate from the hot plasma region which heats the substrate. This heat flux was calculated from the model as shown in Figure 44. To maintain the desired substrate temperature of 1200 K, active cooling is typically required because the heat flux would otherwise drive the substrate temperature well beyond its optimal value. In experimental setups, the substrate may be placed on a cooled stage, for example, to extract excess heat and maintain thermal stability. This cooling, however, would need to be nonuniform to accommodate the nonuniformity of the heat flux to the substrate. More cooling would be needed near the centerline of the reactor compared with further out radially. This is due to the nonuniformity of the temperature profile. If a more uniform power can be achieved, then the cooling requirements would also be more uniform.

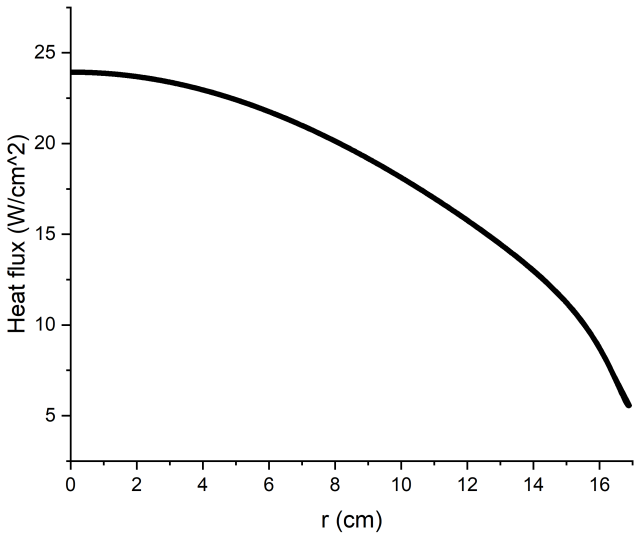

Figure 44: Radial profile of heat flux to the substrate surface.

3.10 Combined effects for optimized growth

When individually tested, there are several factors that improve the uniformity and magnitude of growth rate and defect ratio. Two effects that dramatically improve uniformity are using a uniform power deposition and higher inlet flow rates. Improvements in magnitude are caused by higher inlet flow rates and higher magnitude of power deposition. These three effects also improved the magnitude and uniformity of the defect ratio. A combination of these effects was run to observe an optimal case of diamond growth. The resulting growth rate, defect ratio, H concentration, and CH_3 concentration are compared to the base case and presented in Figures 45 - 48. Combining these effects leads to a highly uniform growth rate and defect ratio out to 15 cm radially, where the magnitudes are enhanced beyond what any one effect can produce individually. Based on these results, it is recommended to design a reactor that includes a combination of uniform power deposition, high-magnitude power deposition, and high inlet flow rates.

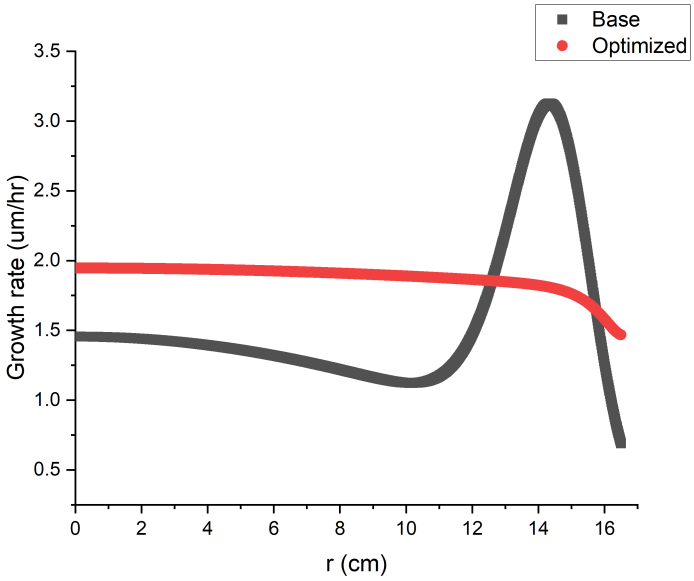

Figure 45: Radial growth rate profile near substrate surface for optimized simulation.

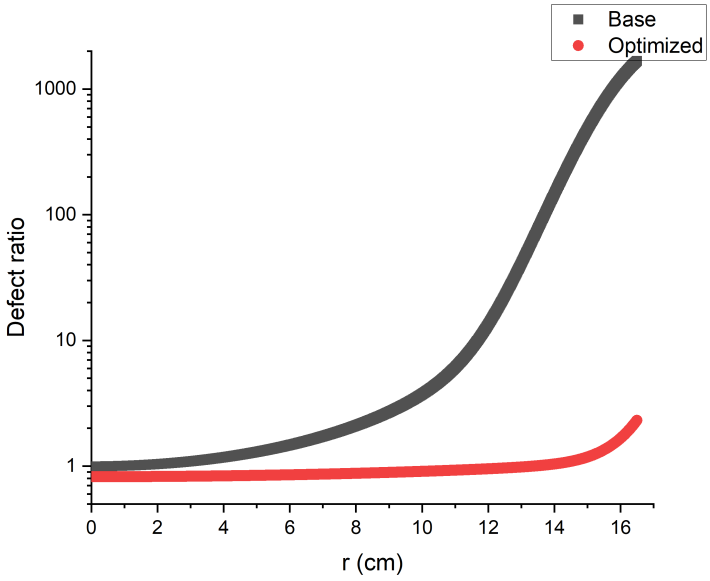

Figure 46: Radial defect ratio profile near substrate surface for optimized simulation.

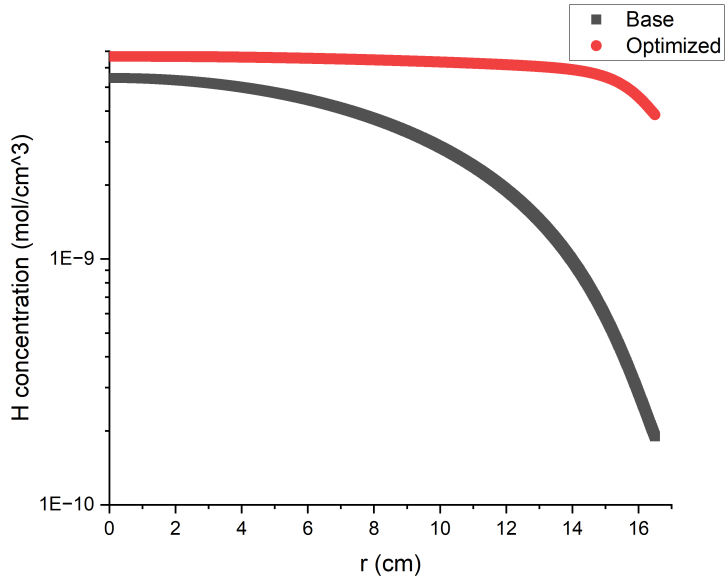

Figure 47: Radial H concentration profile near substrate surface for optimized simulation.

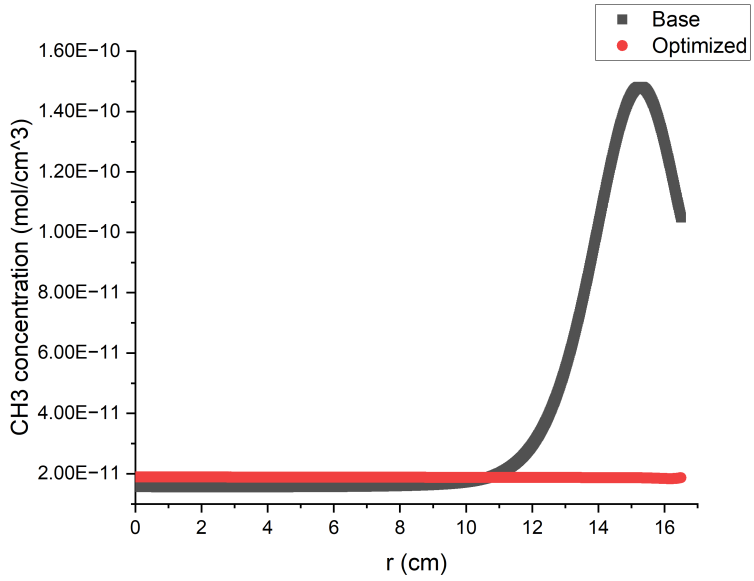

Figure 48: Radial CH_3 concentration profile near substrate surface for optimized simulation.

4 Conclusion

This thesis presents a comprehensive model of a parallel plate CVD reactor for thin film diamond growth, incorporating species transport, temperature-dependent fluid flow, and reduced plasma chemistry. A key focus is the analysis of chemical species relative to thermal equilibrium. While CH_3 and CH_4 remain in equilibrium as confirmed by simplified kinetic rate expressions, H and H_2 exhibit significant deviations. These deviations arise from the fast diffusion and relatively slow reaction kinetics of H, as shown through Damkohler number analysis. As a result, CH_3 and CH_4 concentrations are affected by the nonequilibrium of H, particularly near the substrate, despite themselves being equilibrated. This insight highlights the importance of understanding transport-limited species behavior when predicting growth outcomes.

Simulations reveal that enhancing growth uniformity and magnitude requires improved transport of CH_3 and H to the substrate. High flow rates and more uniform power deposition shift species distributions radially and reduce spatial variation in the growth rate and defect ratio. Compared with MPCVD reactors, the parallel plate configuration offers superior CH_4 utilization, though at a higher power cost. An optimized reactor design combining high flow rate, uniform and increased power deposition leads to significantly improved and more uniform growth. These findings contribute to the design of more efficient, large-area diamond growth systems for advanced materials applications.

References

[1] R A Khmelnitskiy. Prospects for the synthesis of large single-crystal diamonds. *Physics-Uspekhi*, 58(2):134–149, 2015. doi: 10.3367/ufne.0185.201502b.0143.

[2] Awadesh Kumar Mallik. Microwave plasma cvd grown single crystal diamonds–a. *Journal of Coating Science and Technology*, 3(2), 2016.

[3] Top 10 thermally conductive materials, Jun 2021. URL `https://thermtest.com/thermal-resources/top-10-resources/top-10-thermally-conductive-materials`.

[4] MM Antonijevic and MB Petrovic. Copper corrosion inhibitors. a review. *International journal of electrochemical science*, 3(1):1–28, 2008.

[5] Che-Hsin Lin. *Oxidation (of Silicon)*, pages 1584–1584. Springer US, Boston, MA, 2008. ISBN 978-0-387-48998-8. doi: 10.1007/978-0-387-48998-8_1173. URL `https://doi.org/10.1007/978-0-387-48998-8_1173`.

[6] Milton Ohring. *Chapter 6: Chemical Vapor Deposition*, page 277–355. 2 edition, 2002.

[7] Ronald G Munro. Material properties of titanium diboride. *Journal of Research of the National institute of standards and Technology*, 105(5):709, 2000.

[8] Optical constants of glass. URL `https://refractiveindex.info/?shelf=3d&book=glass&page=BK7`.

[9] Christopher Mims. One of the world's biggest diamonds could be key to some of the world's fastest microchips. *The Wall Street Journal*, Nov 2023.

[10] V Mortet, A Taylor, M Davydova, M Lamač, N Lambert, I Elantyev, J Lorinčík, David Troadec, M Vronka, and S Potockỳ. Effect of pulsed methane gas flow on the incorporation of phosphorous in diamond. *Diamond and Related Materials*, 124:108928, 2022.

[11] Catherine Rond, Rania Salem, Stephan Hamann, Guillaume Lombardi, Jürgen Röpcke, and Alix Gicquel. Chemical analysis of h2–b2h6 and h2–ch4–b2h6 microwave cvd plasmas used for diamond deposition. *Plasma Sources Science and Technology*, 25(2):025016, 2016.

[12] FG Celii and JE Butler. Diamond chemical vapor deposition. *Annual Review of Physical Chemistry*, 42(1):643–684, 1991.

[13] Scott S Dossa, Ilya Ponomarev, Boris N Feigelson, Marc Hainke, Christian Kranert, Jochen Friedrich, and Jeffrey J Derby. Analysis of the high-pressure high-temperature (hpht) growth of single crystal diamond. *Journal of Crystal Growth*, 609:127150, 2023.

[14] PM Martineau, MP Gaukroger, KB Guy, SC Lawson, DJ Twitchen, I Friel, JO Hansen, GC Summerton, TPG Addison, and R Burns. High crystalline quality single crystal chemical vapour deposition diamond. *Journal of Physics: Condensed Matter*, 21(36):364205, 2009.

[15] Yuri A Mankelevich, Michael NR Ashfold, and Jie Ma. Plasma-chemical processes in microwave plasma-enhanced chemical vapor deposition reactors operating with c/h/ar gas mixtures. *Journal of applied physics*, 104(11), 2008.

[16] JE Butler, Yu A Mankelevich, A Cheesman, Jie Ma, and MNR Ashfold. Understanding the chemical vapor deposition of diamond: recent progress. *Journal of Physics: Condensed Matter*, 21(36):364201, 2009.

[17] Alastair Stacey, Igor Aharonovich, Steven Prawer, and James E Butler. Controlled synthesis of high quality micro/nano-diamonds by microwave plasma chemical vapor deposition. *Diamond and related materials*, 18(1):51–55, 2009.

[18] Qi Liang, Cheng Yi Chin, Joseph Lai, Chih-shiue Yan, Yufei Meng, Ho-kwang Mao, and Russell J. Hemley. Enhanced growth of high quality single crystal diamond by microwave plasma assisted chemical vapor deposition at high gas pressures. *Applied Physics Letters*, 94 (2), 2009. doi: 10.1063/1.3072352.

[19] Jerome A. Cuenca, Soumen Mandal, Evan L.H. Thomas, and Oliver A. Williams. Microwave plasma modelling in clamshell chemical vapour deposition diamond reactors. *Diamond and Related Materials*, 124:108917, 2022. doi: 10.1016/j.diamond.2022.108917.

[20] F Silva, J Achard, O Brinza, X Bonnin, K Hassouni, A Anthonis, K De Corte, and J Barjon. High quality, large surface area, homoepitaxial mpacvd diamond growth. *Diamond and Related Materials*, 18(5-8):683–697, 2009.

[21] Seiichiro Matsumoto, Yoshiki Asakura, and Kenji Hirakuri. Diamond synthesis by using very high frequency plasmas in parallel plate electrodes configuration. *Applied physics letters*, 71 (18):2707–2709, 1997.

[22] David G Goodwin. Scaling laws for diamond chemical-vapor deposition. i. diamond surface chemistry. *Journal of Applied Physics*, 74(11):6888–6894, 1993.

[23] Hydrogen Atom, . URL `https://webbook.nist.gov/cgi/cbook.cgi?ID=C12385136&Mask=1&Type=JANAFG&Table=on`.

[24] Hydrogen, . URL `https://webbook.nist.gov/cgi/cbook.cgi?ID=C1333740&Mask=1&Type=JANAFG&Table=on`.

[25] Normand C Blais and Joseph B Mann. Thermal conductivity of helium and hydrogen at high temperatures. *The Journal of Chemical Physics*, 32(5):1459–1465, 1960.

[26] Lev N Krasnoperov, Ilia J Kalinovski, Hae Nuh Chu, and David Gutman. Heterogeneous reactions of hydrogen atoms and methyl radicals with a diamond surface in the 300-1133 k temperature range. *The Journal of Physical Chemistry*, 97(45):11787–11796, 1993.

[27] K Hassouni, A Gicquel, M Capitelli, and J Loureiro. Chemical kinetics and energy transfer in moderate pressure h2 plasmas used in diamond mpacvd processes. *Plasma Sources Science and Technology*, 8(3):494, 1999.

[28] Carl D Scott, Samir Farhat, Alix Gicquel, Khaled Hassouni, and Michel Lefebvre. Determining electron temperature and density in a hydrogen microwave plasma. *Journal of thermophysics and heat transfer*, 10(3):426–435, 1996.

[29] Cantera. URL `https://cantera.org/`.

[30] COMSOL Multiphysics. URL `https://www.comsol.com/`.

[31] Kristin Paragian. Thin film diamond. Manuscript submitted for publication. Department of Chemical and Biological Engineering, Princeton University. Princeton University Library, Master's Thesis Collection, 2025.

[32] Michael NR Ashfold and Yuri A Mankelevich. Two-dimensional modeling of diamond growth by microwave plasma activated chemical vapor deposition: Effects of pressure, absorbed power and the beneficial role of nitrogen on diamond growth. *Diamond and Related Materials*, 137:110097, 2023.

[33] Sydney Chapman and T G Cowling. *The Mathematical Theory of Non-uniform Gases: An Account of the Kinetic Theory of Viscosity, Thermal Conduction and Diffusion in Gases*. Cambridge University Press, 3 edition, 1991.

[34] Ahren W Jasper and James A Miller. Lennard–jones parameters for combustion and chemical kinetics modeling from full-dimensional intermolecular potentials. *Combustion and Flame*, 161(1):101–110, 2014.

Appendices

A Additional equation information

With the assumptions that (1) the gas molecules can be described as hard spheres and (2) the gas is dilute in molecular hydrogen, the binary diffusion coefficient proposed by Chapman and Enskog can be used for the diffusion coefficient of each species s in H_2 [33]:

$$D_{s,H_2} = \frac{3}{8N\sigma_{s,H_2}^2}\sqrt{\frac{k_B T}{2\pi}(\frac{1}{m_s}+\frac{1}{m_{H_2}})} \tag{15}$$

where σ_{s,H_2}, m_s and m_{H2} are the collision diameter of species s and H_2, mass of species s, and mass of H_2, respectively. The collision diameter is the average of the distance parameters σ_s and σ_{H_2} [34]:

$$\sigma_{s,H_2} = \frac{\sigma_s + \sigma_{H_2}}{2} \tag{16}$$

B Comparison of model species densities to the literature

A comparison of the axial densities of H and CH_3 with literature data is shown in Figures 49 and 50 [20].

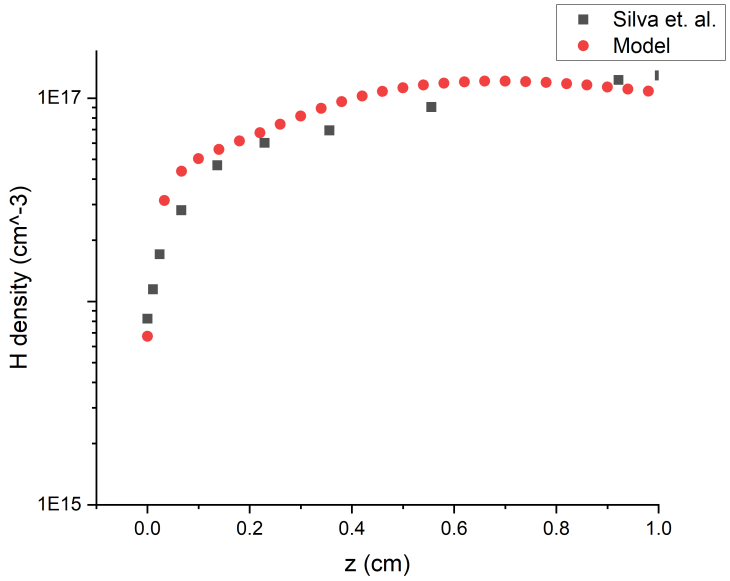

Figure 49: Axial density profile of H from the model compared with literature data [20] within 1 *cm* of the substrate.

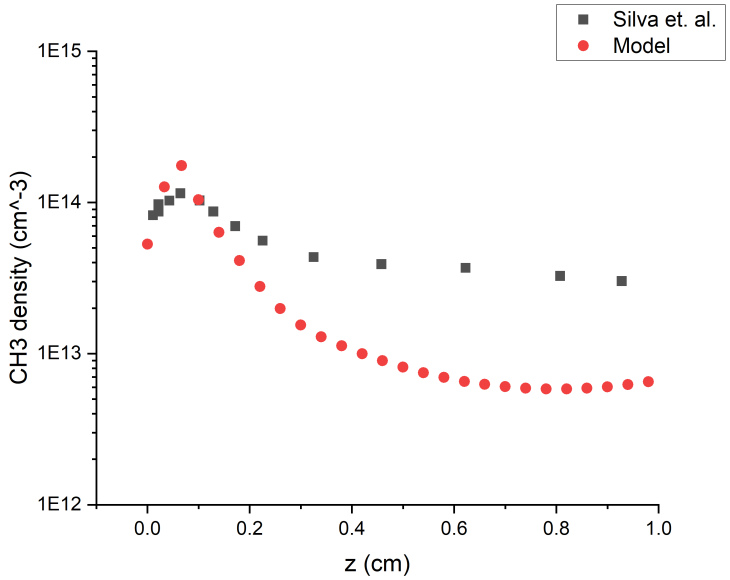

Figure 50: Axial density profile of CH_3 from the model compared with literature data [20] within 1 *cm* of the substrate.

C 2D mole fractions profiles of CH_2, CH, C, C_2H, C_2H_4, C_2H_5, and C_2H_6

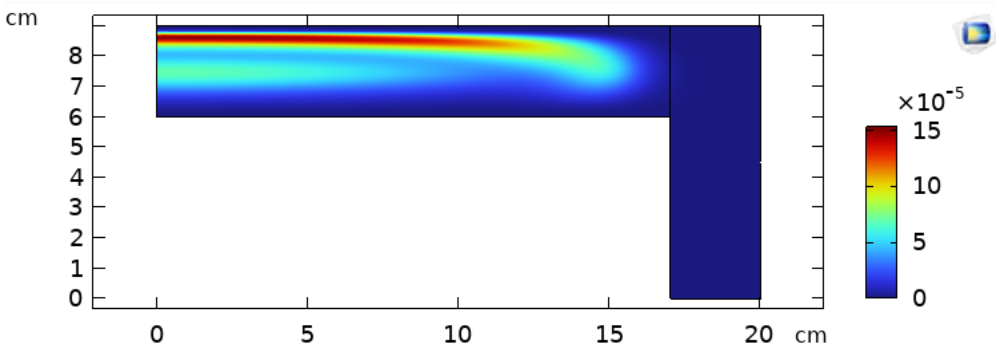

Figure 51: Mole fraction of CH_2 for base case simulation.

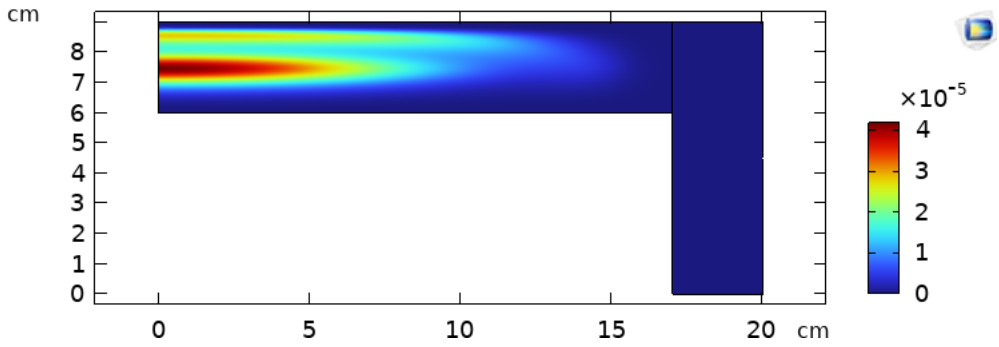

Figure 52: Mole fraction of CH for base case simulation.

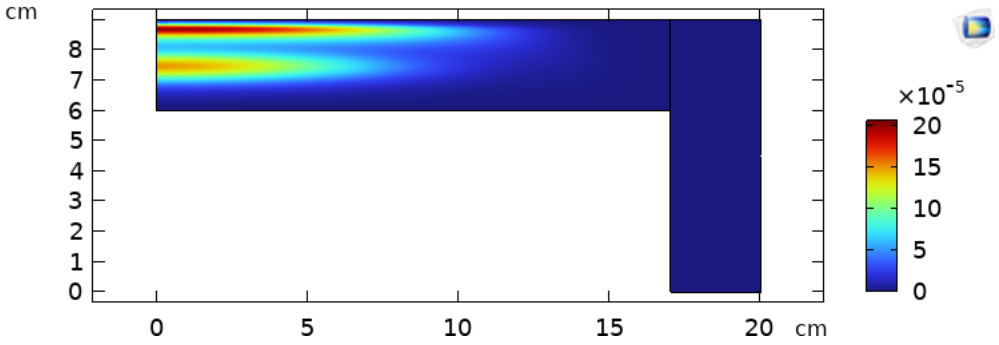

Figure 53: Mole fraction of C for base case simulation.

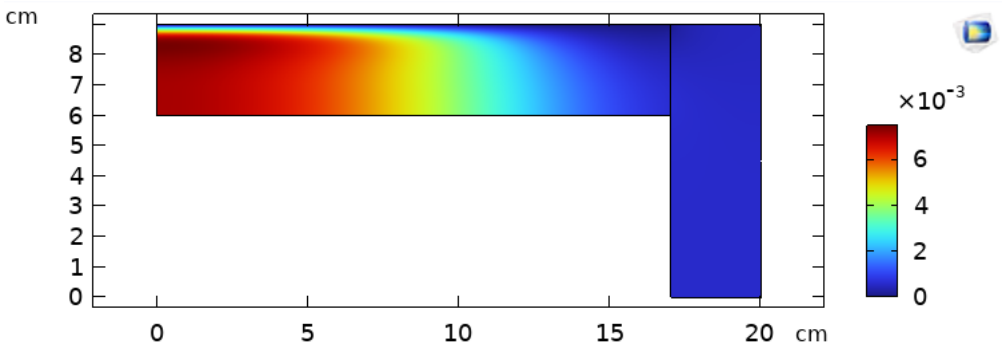

Figure 54: Mole fraction of C_2H for base case simulation.

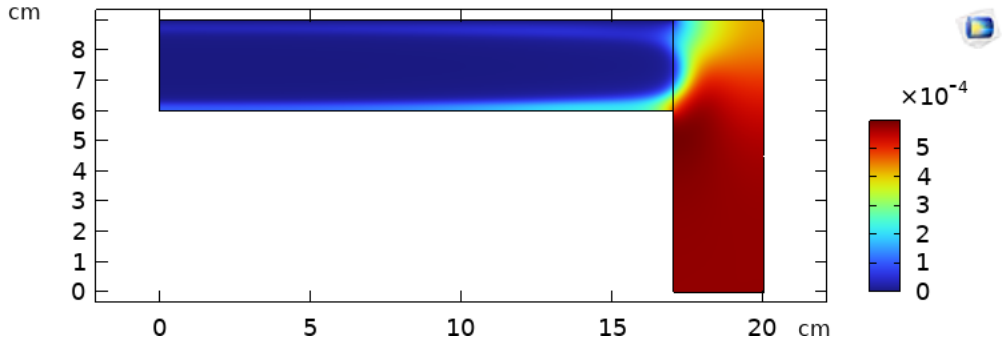

Figure 55: Mole fraction of C_2H_4 for base case simulation.

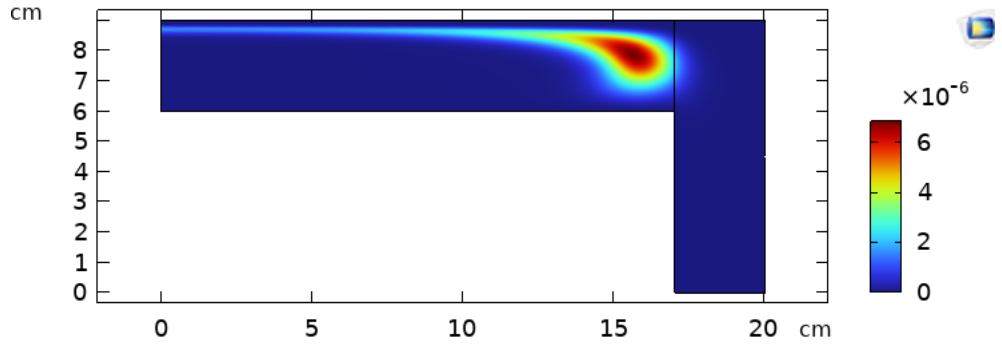

Figure 56: Mole fraction of C_2H_5 for base case simulation.

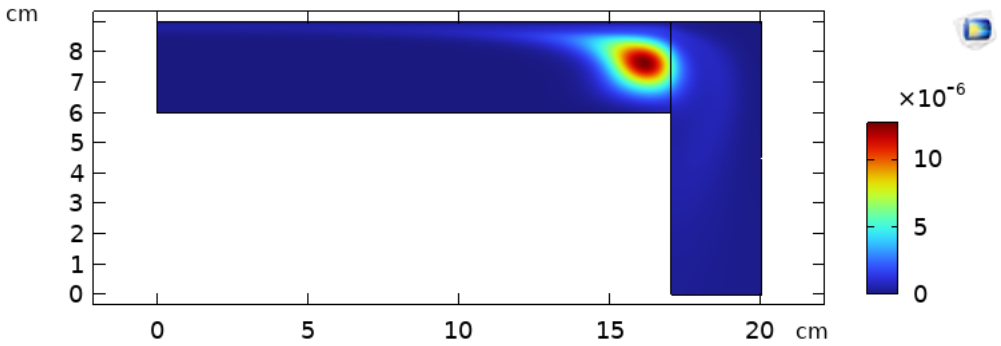

Figure 57: Mole fraction of C_2H_6 for base case simulation.